

1 **A broadly neutralizing antibody protects against SARS-CoV, pre-emergent bat CoVs, and**
2 **SARS-CoV-2 variants in mice**

3
4 David R. Martinez^{1,7}, Alexandra Schaefer^{1,7}, Sophie Gobeil^{2,7}, Dapeng Li^{2,7}, Gabriela De la
5 Cruz³, Robert Parks², Xiaozhi Lu², Maggie Barr², Kartik Manne², Katayoun Mansouri²,
6 Robert J. Edwards², Boyd Yount¹, Kara Anasti², Stephanie A. Montgomery⁴, Shaunna Shen⁶,
7 Tongqing Zhou⁵, Peter D. Kwong⁵, Barney S. Graham⁵, John R. Mascola⁵, David. C.
8 Montefiori⁶, Munir Alam², Gregory D. Sempowski², Kevin Wiehe², Kevin O. Saunders^{2,6},
9 Priyamvada Acharya^{2,6,*}, Barton F. Haynes^{2,*}, Ralph S. Baric^{1,*}.

10
11 ¹ Department of Epidemiology, University of North Carolina at Chapel Hill, Chapel Hill, NC,
12 USA

13 ² Duke Human Vaccine Institute, Duke University School of Medicine, Durham, NC, USA

14 ³ Lineberger Comprehensive Cancer Center, University of North Carolina School of Medicine,
15 Chapel Hill, NC, USA

16 ⁴ Department of Laboratory Medicine and Pathology, University of North Carolina School of
17 Medicine, Chapel Hill, NC, USA

18 ⁵ Vaccine Research Center, National Institute of Allergy and Infectious Diseases, NIH, Bethesda,
19 MD, USA

20 ⁶ Department of Surgery, Duke University School of Medicine, Durham, NC, USA

21

22 ⁷ These authors contributed equally.

23

24 *Corresponding authors.

25 Priyamvada Acharya, P.A., priyamvada.acharya@duke.edu

26 Barton F. Haynes, B.F.H., barton.haynes@duke.edu

27 Ralph S. Baric, R.S.B., rbaric@email.unc.edu

28 **Keywords:** SARS-CoV-2 D614G, B.1.1.7, B.1.429, B1.351, SARS-like virus, *Sarbecovirus*,

29 countermeasures, DH1047 antibody, bNAb, panCoV

30

31 **Abstract**

32 SARS-CoV in 2003, SARS-CoV-2 in 2019, and SARS-CoV-2 variants of concern

33 (VOC) can cause deadly infections, underlining the importance of developing broadly effective

34 countermeasures against Group 2B Sarbecoviruses, which could be key in the rapid prevention

35 and mitigation of future zoonotic events. Here, we demonstrate the neutralization of SARS-CoV,

36 bat CoVs WIV-1 and RsSHC014, and SARS-CoV-2 variants D614G, B.1.1.7, B.1.429, B1.351

37 by a receptor-binding domain (RBD)-specific antibody DH1047. Prophylactic and therapeutic

38 treatment with DH1047 demonstrated protection against SARS-CoV, WIV-1, RsSHC014, and

39 SARS-CoV-2 B1.351 infection in mice. Binding and structural analysis showed high affinity

40 binding of DH1047 to an epitope that is highly conserved among Sarbecoviruses. We conclude

41 that DH1047 is a broadly neutralizing and protective antibody that can prevent infection and

42 mitigate outbreaks caused by SARS-like strains and SARS-CoV-2 variants. Our results argue

43 that the RBD conserved epitope bound by DH1047 is a rational target for pan Group 2B

44 coronavirus vaccines.

45

46 **Introduction**

47 The emergence of severe acute respiratory syndrome (SARS-CoV) in 2003 led to more
48 than 8,000 infections and 800 deaths ^{1,2}. In 2012, the Middle East Respiratory Syndrome
49 (MERS-CoV) emerged in Saudi Arabia ³, which has so far infected ~2,600 people and caused
50 900 deaths. Less than a decade following the emergence of MERS-CoV, SARS-CoV-2 emerged
51 in Wuhan, China ⁴. The spread of SARS-CoV-2, the virus that causes coronavirus disease of
52 2019 (COVID-19) was rapid, and by March 2020, the World Health Organization (WHO) had
53 declared SARS-CoV-2 a global pandemic. By April 2021, more than 140 million people had
54 been infected globally, resulting in >3 million deaths. Therefore, there is a need to develop safe
55 and effective broad-spectrum countermeasures that can prevent the rapid spread and attenuate the
56 severe disease outcomes associated with current and future SARS-like virus emergence events.

57 Human highly pathogenic CoV outbreaks are likely of bat origin ⁵, and there is great
58 genetic diversity among bat SARS-like viruses ⁶. Zoonotic CoVs of bat origin, such as
59 RsSHC014 and WIV-1, can utilize the human ACE2 receptor for cell entry and infect human
60 airway cells ^{7,8}, underlining their potential for emergence in naïve human populations. Moreover,
61 existing SARS-CoV therapeutic monoclonal antibodies and SARS-CoV-2 mRNA vaccines do
62 not protect against zoonotic SARS-like virus infection ⁷⁻⁹. Given the pandemic potential of
63 SARS-like viruses, the development of broadly effective countermeasures, such as universal
64 vaccination strategies ⁹⁻¹¹, and coronavirus (CoV) cross-reactive monoclonal antibodies is a
65 global health priority. Moreover, given the emergence of the SARS-CoV-2 variants that are
66 partially or fully resistant to some neutralizing antibodies authorized for COVID-19 treatment ¹²⁻
67 ¹⁴, there is a need to discover mAb therapies that are broadly effective against the SARS-CoV-2
68 variants and zoonotic SARS-like viruses that will continue to emerge in the future.

69 The receptor binding domain (RBD) of SARS-CoV-2 is one of the targets for highly
70 potent neutralizing antibodies. Despite the high degree of genetic diversity within the RBD in
71 SARS-like viruses ⁶, antibodies can be engineered to recognize diverse SARS-like viruses.
72 Rappazzo *et al.* recently reported that an engineered RBD-directed antibody, ADG-2, neutralized
73 SARS-like viruses and protected against SARS-CoV and wild type SARS-CoV-2 ¹⁵. Therefore,
74 the RBD of Sarbecoviruses contains conserved epitopes that are the target of broadly
75 neutralizing antibodies. In agreement with the notion that the RBD contains a conserved epitope
76 shared among SARS, SARS-like, SARS-CoV-2 and the variants, we have identified a panCoV
77 protective antibody: DH1047. Here, we demonstrate, using both pseudoviruses and live virus
78 assays, that DH1047 neutralizes SARS-CoV, SARS-like bat viruses RsSHC014 and WIV-1, and
79 SARS-CoV-2 D614G, B.1.1.7, B.1.429, B.1.351 variants. Structural analysis shows that
80 DH1047 targets a highly conserved RBD region among the Sarbecoviruses. Importantly, we also
81 demonstrate that DH1047 provides prophylactic and therapeutic protection activity against
82 pathogenic SARS-CoV, RsSHC014, WIV-1, wild type SARS-CoV-2, and against a pathogenic
83 B.1.351 variant in mice. Thus, DH1047 is a pan-group 2B CoV protective antibody that can be
84 used to prevent and treat SARS-CoV-2 infections including important with variants of concern
85 and has the potential to prevent disease from a future outbreak of a pre-emergent, zoonotic
86 SARS-like virus strains that jump into naïve animal and human populations.

87

88 **Results**

89 **The identification of broadly cross-binding and neutralizing antibodies**

90 We previously isolated 1737 monoclonal antibodies (mAbs) from a SARS-CoV
91 convalescent patient 17 years following infection and a SARS-CoV-2 convalescent patient from

92 36 days post infection¹⁶. From this large panel of mAbs previously described by Li *et al.* we
93 focused on 50 cross-reactive antibodies which bound to SARS-CoV, SARS-CoV-2, and other
94 human and animal CoV antigens¹⁶. To examine if these cross-reactive mAbs neutralized
95 divergent Sarbecoviruses, we measured neutralizing activity against a mouse-adapted SARS-
96 CoV-2 2AA mouse-adapted (MA) virus, SARS-CoV, bat CoV WIV-1, and bat CoV RsSHC014
97 using live viruses, and found four broadly cross-reactive antibodies, DH1235, DH1073,
98 DH1046, and DH1047 (Fig. 1). DH1235 neutralized SARS-CoV-2 2AA MA, SARS-CoV, and
99 bat CoV WIV-1 with IC₅₀ of 0.122, 0.0403, and 0.060 µg/ml, respectively (Fig. 1A and Table
100 S1). DH1073 neutralized SARS-CoV-2 2AA MA, SARS-CoV, and bat CoV WIV-1 with IC₅₀ of
101 0.808, 0.016, and 0.267 µg/ml, respectively (Fig. 1B and Table S1). DH1046 neutralized SARS-
102 CoV-2 2AA MA, SARS-CoV, bat CoV WIV-1, and bat CoV RsSHC014 with IC₅₀ of 2.85,
103 0.103, 0.425, and 1.27µg/ml, respectively (Fig. 1C and Table S1). Similar to DH1046, DH1047
104 more potently neutralized SARS-CoV-2 2AA MA, SARS-CoV, bat CoV WIV-1, and bat CoV
105 RsSHC014 with IC₅₀ of 0.397, 0.028, 0.191, and 0.200µg/ml, respectively (Fig. 1D and Table
106 S1).

107 We also measured binding responses for DH1235, DH1073, DH1046, and DH1047
108 against zoonotic bat RaTG13-CoV, bat RsSHC014, and Pangolin GXP4L-CoV spikes. DH1235,
109 DH1073, DH1046, and DH1047 mAbs showed strong binding to bat RaTG13-CoV, bat
110 RsSHC014, and pangolin GXP4L-CoV spikes in addition to SARS-CoV and SARS-CoV-2 (Fig.
111 1E-1H). Finally, DH1235, DH1073, DH1046, and DH1047 bound to SARS-CoV-2 RBD and did
112 not bind to the SARS-CoV-2 NTD, demonstrating specific binding to the RBD. While DH1235,
113 DH1073, DH1046, and DH1047 were cross-reactive against epidemic, pandemic, and zoonotic
114 Sarbecovirus spikes, they did not bind to MERS-CoV, HuCoV OC43, HuCoV NL63, and

115 HuCoV 229E spike proteins (Fig. S1), suggesting these mAbs recognize a conserved epitope
116 found only in Group 2B betacoronaviruses. By Negative Stain Electron Microscopy (NSEM), we
117 observed binding of DH1047 to the RBD of bat RsSHC014 and SARS-CoV spike ectodomains,
118 with overall similar orientations as was observed for DH1047 binding to the SARS-CoV-2 spike
119 ectodomain (Figure S2) ¹⁶.

120 Finally, DH1235, DH1073, DH1046, and DH1047 exhibited medium to long heavy-
121 chain-complementarity-determining-region 3 (HCDR3) lengths and variable somatic mutation
122 rates in the heavy chain genes. DH1235, DH1073, and DH1046, had HCDR3 lengths of 21, 15,
123 and 24, and somatic hypermutation (SMH) rates of 1.7, 9.0, and 4.7, respectively (Table S2). The
124 most potent neutralizing antibody DH1047 had HCDR3 lengths and SMH rates of 24 and 8.05,
125 respectively (Table S2).

126

127 **The protective activity of DH1235, DH1073, DH1046, and DH1047 against SARS-CoV**

128 To define the protective efficacy of these four RBD-specific IgG bNAbs, we passively
129 immunized aged mice with DH1235, DH1073, DH1046, DH1047 and a negative control
130 influenza mAb, CH65 ¹⁷, at 10mg/kg 12 hours prior to infection and evaluated lung viral titer
131 replication. Neither DH1235, DH1073, nor DH1046 protected against SARS-CoV mouse-
132 adapted passage 15 (MA15) challenge in mice and all had lung viral replication comparable to
133 that of control mice (Fig. 2A). In contrast, prophylactic administration of DH1047 fully protected
134 mice from lung viral titer replication (Fig. 2A). Given the prophylactic potential of DH1047, we
135 sought to also evaluate its therapeutic potential in a highly sensitive and stringent aged mouse
136 model. We treated mice with control mAb and DH1047 at 10mg/kg both at 12 hours before and
137 12 hours post infection with SARS-CoV MA15 and monitored mice for signs of clinical disease,

138 including weight loss, pulmonary function, which was measured by whole-body
139 plethysmography (Buxco), through day 4 post infection (d4pi). In agreement with the SARS-
140 CoV MA15 experiments, prophylactic treatment with DH1047 protected mice from weight loss
141 through d4pi (Fig. 2B), and also protected mice from lung viral replication (Fig. 2C). We also
142 evaluated if the prophylactic and therapeutic administration of DH1047 protected against lung
143 pathology as measured by 1) lung discoloration, which is a visual metric of gross lung damage
144 taken at the time of the necropsy, 2) microscopic evaluation as measured by an acute lung injury
145 (ALI) scheme, and 3) a diffuse alveolar damage (DAD) scheme. ALI and DAD, which are
146 characterized by histopathologic changes including alveolar septal thickening, protein exudate in
147 the airspace, hyaline membrane formation, and neutrophils in the interstitium or alveolar sacs,
148 were both blindly evaluated by a board-certified veterinary pathologist. The prophylactic
149 administration of DH1047 resulted in complete protection from macroscopic lung discoloration
150 (Fig. 2D) and microscopic lung pathology as measured by ALI (Fig. 2E and Fig. S3) and DAD
151 (Fig. 2F and Fig. S3). Similarly, the therapeutic administration of DH1047 12 hours post
152 infection resulted in reductions in lung viral titers (Fig. 2C and Fig. S3) as well as the
153 macroscopic lung damage measured by the lung discoloration score (Fig. 2D and Fig. S3). In
154 contrast to the prophylactic treatment condition, therapeutic administration of DH1047 did not
155 significantly reduce microscopic lung pathology compared to control mice as measured by ALI
156 (Fig. 2E and Fig. S3) and DAD (Fig. 2F and Fig. S3) in this highly susceptible model for SARS-
157 CoV pathogenesis. Thus, DH1047 can prevent SARS-CoV disease when administered
158 prophylactically and has early measurable therapeutic benefits in highly susceptible aged mouse
159 models, much like other SARS-CoV-2 therapeutic neutralizing antibodies which have the most
160 benefit in outpatient settings^{4,18,19}.

161

162 **Cryo-EM structure of the SARS-CoV/DH1047 complex**

163 To visualize the binding epitope of DH1047 and to compare with the previously reported
164 structure of the complex with the SARS-CoV-2 spike ectodomain¹⁶, we solved the cryo-EM
165 structure of SARS-CoV bound to DH1047. 3D-classification of the cryo-EM dataset resulted in a
166 3.20 Å resolution reconstruction showing three DH1047 Fab bound to each of the 3 RBD of the
167 ectodomain in the “up” position (1 Fab:1 RBD ratio) (Fig. 3, Figure S5 and Table S3). Similar to
168 what we had observed for the DH1047 complex with the SARS-CoV-2 spike ectodomain¹⁶,
169 there was considerable heterogeneity in the RBD region; further classification of particles was
170 performed to better resolve the antibody binding interface, resulting in an asymmetric
171 reconstruction of a population refined to a resolution of 3.4 Å that was used for model fitting.
172 The angle of approach and footprint of DH1047 on the SARS-CoV RBD closely resembled that
173 in the SARS-CoV-2 complex with steric overlap predicted with ACE2 binding (Figure 3A-C).
174 These results demonstrate that DH1047 binds to SARS-CoV and SARS-CoV-2 spike
175 ectodomains by involving homologous interactions, consistent with our analysis of RBD
176 sequence variability that showed a high degree of convergence of the DH1047 epitope¹⁰, thereby
177 defining an RBD conserved site of vulnerability among Sarbecoviruses. The DH1047 epitope on
178 the SARS-CoV-2 RBD is distinct from other known antibodies of Classes 1, 2, 3 and 4 (Figure
179 3D). The DH1047 epitope overlays with that of antibody ADG-2, yet the two epitopes are
180 distinct, and related by a rotation about the Fab longitudinal axis that pivots the ADG-2 antibody
181 more towards the ACE2 binding region (Figures 3D and S6). Finally, we defined the binding
182 affinity of DH1047 against epidemic and zoonotic spike proteins. We measured binding on and
183 off rates against both SARS-CoV and RsSHC014-CoV spike proteins via surface plasmon

184 resonance (SPR). DH1047 bound to the SARS-CoV and RsSCH014-CoV spikes with high
185 affinity, association rates ($> 8.60 \times 10^4 \text{ M}^{-1} \text{ s}^{-1}$) and dissociation rates ($< 1.0 \times 10^{-5} \text{ s}^{-1}$) (Fig. S4),
186 demonstrating that DH1047 binds tightly to both the epidemic SARS-CoV and pre-emergent bat
187 CoVs that are poised for human emergence.

188

189 **The prophylactic and therapeutic activity of DH1047 against bat pre-emergent CoVs and**
190 ***in vitro* neutralization activity against the SARS-CoV-2 variants**

191 As DH1047 neutralized both the pre-emergent bat CoVs WIV-1 and RsSHC014 (Fig. 1),
192 we sought to define if DH1047 had prophylactic and therapeutic efficacy in mice. We evaluated
193 the protective efficacy against lung viral replication against these pre-emergent bat CoVs. We
194 administered DH1047 prophylactically 12 hours before infection and therapeutically 12 hours
195 post infection at 10mg/kg in mice infected with bat CoVs. Importantly, the prophylactic
196 administration of DH1047 completely protected mice from WIV-1 lung viral replication and
197 reduced lung viral titers in therapeutically treated mice compared to control mice (Fig. 4A).
198 Similarly, the prophylactic administration of DH1047 completely protected mice from
199 RsSHC014 lung viral replication and significantly reduced viral replication to near undetectable
200 levels in therapeutically treated mice (Fig. 4B). While we previously demonstrated the
201 prophylactic and therapeutic efficacy of DH1047 against the wild type SARS-CoV-2 in
202 cynomolgus macaques¹⁶, which exhibit mild SARS-CoV-2 disease²⁰, it was not known if the
203 mutations present in the newly emerging SARS-CoV-2 variants would ablate the neutralizing
204 activity of DH1047. We therefore evaluated if DH1047 could neutralize the prevalent variants of
205 concern (VOCs): SARS-CoV-2 D614G, SARS-CoV-2 UK B.1.1.7., SARS-CoV-2 California
206 B1.429, and SARS-CoV South Africa B1.351 using both pseudovirus and live virus

207 neutralization assays. DH1047 neutralized all tested variants of concern with substantial potency
208 (Fig. 4C and Fig. 4D). Pseudovirus neutralization assays revealed strong neutralization of
209 DH1047 against the SARS-CoV-2 VOCs (Fig. 4D). Importantly, live virus neutralization also
210 demonstrated the broadly neutralizing activity of DH1047 with IC₅₀ values against D614G,
211 B.1.1.7, and B.1.351 were 0.059, 0.081, and 0.111µg/ml, respectively.

212

213 **The prophylactic and therapeutic activity of DH1047 against SARS-CoV-2 B.1.351 in mice**

214 Given that the B.1.351 South African variant is more resistant to both vaccine-elicited
215 neutralizing antibodies^{14,21}, and completely ablates the neutralizing activity of the Eli Lilly
216 therapeutic monoclonal antibody LY-CoV555¹², we also sought to evaluate if DH1047 had both
217 prophylactic and therapeutic efficacy against SARS-CoV-2 B.1.351, which incorporates the
218 B.1.351 spike in the SARS-CoV MA10 genome backbone²². We again utilized a highly
219 susceptible and vulnerable aged mouse model in the SARS-CoV-2 B.1.351 protection
220 experiments. Consistent with the SARS-CoV, WIV-1, and RsSHC014 *in vivo* data, the
221 prophylactic administration of DH1047 mediated protection against severe weight loss following
222 SARS-CoV-2 B.1.351 challenge in aged mice (Fig. 5A). In contrast, we did not observe
223 differences in weight loss from the therapeutic administration of DH1047 (Fig. 5A). Mice
224 prophylactically treated with DH1047 had undetectable levels of SARS-CoV-2 B.1.351 lung
225 viral replication (Fig. 5B) and were also completely protected from macroscopic lung pathology
226 compared to controls (Fig. 5C). While we observed no significant protection from weight loss in
227 DH1047 therapeutically treated mice, we did observe a significant reduction in lung viral titers
228 compared to control (Fig. 5B). We also evaluated the microscopic lung pathology as measured
229 by ALI (Fig. 5D) and DAD scoring schemes (Fig. 5E) in this highly susceptible aged model for

230 SARS-CoV-2 B.1.351 pathogenesis. Importantly, the prophylactic administration of DH1047
231 significantly protected mice from lung histopathology as measured by ALI and DAD compared
232 to control mice. Additionally, we observed a reduction in ALI by the therapeutic administration
233 of DH1047 as measure by macroscopic lung pathology (Fig. 5C) and lung histopathology by
234 ALI (Fig. 5D). Therefore, DH1047 can prevent and treat SARS-CoV-2 infections with the
235 B.1.351 variant of concern *in vivo*, especially if given early in infection.

236

237 **Discussion**

238 The emergence of SARS-CoV and SARS-CoV-2 in the last two decades underscores a
239 critical need to develop broadly effective countermeasures against Sarbecoviruses. Moreover,
240 with the recent emergence of more highly transmissible²³, virulent²⁴, and neutralization resistant
241 UK B.1.1.7 variant, that can partially evade existing countermeasures^{12,14}, there is a need to
242 develop next-generation mAb therapeutics that can broadly neutralize these variants, as well as
243 future variants of concern. For example, the SARS-CoV-2 South African B.1.351 variant
244 completely ablates the neutralization activity of the mAb LY-CoV555^{12,13}. As a result, the
245 emergency use authorization (EUA) of LY-CoV555 was recently rescinded by the U.S. Food and
246 Drug Administration (FDA). In addition, the presence of the E484K mutation in many variants
247 of concern, severely dampens the neutralization activity by more than 6-fold of the AstraZeneca
248 COV2-2196 mAb, Bii BioSciences mAb Bii-198, and the Regeneron mAb REGN 10933
249^{13,14,19}. In addition to evading currently monoclonal antibody therapeutics, some of the variants
250 including B.1.351 can diminish the efficacy of clinically approved vaccines, including the
251 Johnson & Johnson single-dose vaccine and the AstraZeneca ChAdOx1^{25,26}. Furthermore, some
252 monoclonal antibodies isolated from vaccine recipients of the Moderna and Pfizer vaccines also

253 demonstrated reduced efficacy against mutations present in the variants²⁷. Therefore, current
254 vaccine and mAb therapies must be monitored in real time to define the performance of existing
255 therapies against newly emerging and spreading variants. In the setting of reduced vaccine
256 efficacy, the deployment of effective mAb therapies against the variants, such as DH1047, could
257 be a strategy to help control the COVID-19 pandemic.

258 The development of universal vaccination strategies against Sarbecoviruses will be
259 improved by the identification and characterization of broadly protective and conserved epitopes
260 across SARS-like virus strains. Recent studies described broadly reactive antibodies that target
261 the subunit 2 (S2) portion of the spike protein²⁸⁻³¹. While the broad recognition of these S2-
262 specific antibodies is encouraging, these antibodies weakly neutralized diverse CoVs. Given the
263 limited characterization of these mAbs, it is unclear if these S2-specific mAbs are broadly
264 protective *in vivo* against diverse epidemic and zoonotic pre-emergent CoVs. In contrast, RBD-
265 specific antibody, S2X259, neutralized SARS-CoV-2 variants and zoonotic SARS-like viruses,
266 as measured by pseudovirus neutralization³². Similarly, a recent subset of RBD-specific cross-
267 reactive mAbs also showed *in vitro* activity³³, although their *in vivo* breadth and protective
268 efficacy remains unconfirmed. It is interesting that DH1235, DH1073, and DH1046 neutralized
269 SARS-CoV but did not protect against SARS-CoV challenge *in vivo*. Perhaps DH1235, DH1073,
270 and DH1046 require 1) non-neutralizing functions for protecting against infection *in vivo*, or 2)
271 have a distinct mode or angle of binding to SARS-CoV compared to DH1047 required for the
272 observed protection. This underlines the importance of performing *in vivo* protection studies in
273 addition to *in vitro* neutralization assays to truly define the protective efficacy of panCoV-
274 specific mAbs.

275 In contrast to ADG-2 which uses VH3-21 for its heavy chain and has a 17 amino acid
276 long HCDR3, DH1047 uses VH1-46 and has a 24 amino acid long HCDR3 (Table S2) ¹⁵.
277 Moreover, ADG-2 and DH1047 have overlapping, yet distinct binding footprints, targeting a
278 conserved region on the RBD (Fig. S6). In addition, the DH1047 epitope is distinct to those from
279 cross-reactive antibodies S309 and CR3022 (Fig. 3D) and targets an epitope near those from
280 class 4 antibodies. DH1047 had broad protective *in vivo* efficacy against pre-emergent SARS-
281 like viruses, epidemic SARS-CoV, and the SARS-CoV-2 B.1.351 variant, underscoring that
282 DH1047 recognizes a pan Sarbecovirus neutralizing epitope. Consistent with this notion, we
283 have described a SARS-CoV-2 RBD-ferritin nanoparticle vaccine that elicited neutralizing
284 antibodies against pre-emergent SARS-like viruses and protected against SARS-CoV-2
285 challenge in monkeys ¹⁰. The serum antibody responses in these SARS-CoV-2 RBD-ferritin
286 nanoparticle-vaccinated monkeys could block DH1047 binding responses against SARS-CoV-2
287 spike proteins, suggesting that SARS-CoV-2 RBD vaccines elicit DH1047-like antibody
288 responses and could potentially protect against the future emergence of SARS- or SARS2-like
289 viruses.

290 Moving forward, it will be critical to closely monitor SARS- and SARS2-like viruses of
291 zoonotic origin and actively monitor if broad-spectrum antibodies like ADG-2, DH1047, and
292 S2X259 retain their inhibitory activity against pre-emergent viruses. We envision a system in
293 which broad-spectrum antibodies like DH1047 could be tested for safety in small Phase I clinical
294 trials so that in the event that a future SARS-like virus emerges, DH1047 could immediately be
295 tested in larger efficacy trials at the site of an outbreak to potentially prevent the rapid spread of
296 an emergent CoV. Moreover, given that DH1047 exhibited strong *in vivo* protection against the
297 SARS-CoV-2 B.1.351 VOC, this mAb could be deployed as a mAb therapeutic to help control

298 the current COVID-19 pandemic. Like other therapeutic antibodies evaluated against COVID19
299 infections, our data argues that early administration will prove critical for protecting against
300 severe disease outcomes ¹⁹. We conclude that DH1047 is a broadly protective mAb that has
301 efficacy against pre-emergent, zoonotic SARS-like viruses from different clades, neutralizes
302 highly transmissible SARS-CoV-2 variants, and protects against SARS-CoV-2 B.1.351.

303

304

305

306

307

308

309

310

311

312

313

314

315

316

317

318

319

320

321

322

323 **Methods**

324 **Antibody isolation**

325 Antibodies were isolated from antigen-specific single B cells as previously described
326 from an individual who had recovered from SARS-CoV-1 infection 17 years prior to
327 leukapheresis, and from a SARS-CoV-2 convalescent individual from 36 days post infection ¹⁶.

328

329 **Measurement of CoV spike binding by ELISA**

330 Indirect binding ELISAs were conducted in 384 well ELISA plates (Costar #3700) coated
331 with 2µg/ml antigen in 0.1M sodium bicarbonate overnight at 4°C, washed and blocked with
332 assay diluent (1XPBS containing 4% (w/v) whey protein/ 15% Normal Goat Serum/ 0.5%
333 Tween-20/ 0.05% Sodium Azide). mAbs were incubated for 60 minutes in three-fold serial
334 dilutions beginning at 100µg/ml followed by washing with PBS/0.1% Tween-20. HRP
335 conjugated goat anti-mouse IgG secondary antibody (SouthernBiotech 1030-05) was diluted to
336 1:10,000 in assay diluent without azide, incubated at for 1 hour at room temperature, washed and
337 detected with 20µl SureBlue Reserve (KPL 53-00-03) for 15 minutes. Reactions were stopped
338 via the addition of 20µl HCL stop solution. Plates were read at 450nm. Area under the curve
339 (AUC) measurements were determined from binding of serial dilutions.

340

341 **Measurement of neutralizing antibodies against live viruses**

342 Full-length SARS-CoV-2 Seattle, SARS-CoV-2 D614G, SARS-CoV-2 B.1.351, SARS-
343 CoV-2 B.1.1.7, SARS-CoV, WIV-1, and RsSHC014 viruses were designed to express

344 nanoluciferase (nLuc) and were recovered via reverse genetics as described previously¹⁶. Virus
345 titers were measured in Vero E6 USAMRIID cells, as defined by plaque forming units (PFU) per
346 ml, in a 6-well plate format in quadruplicate biological replicates for accuracy. For the 96-well
347 neutralization assay, Vero E6 USAMRID cells were plated at 20,000 cells per well the day prior
348 in clear bottom black walled plates. Cells were inspected to ensure confluency on the day of
349 assay. mAbs were serially diluted 3-fold up to nine dilution spots at specified concentrations.
350 Serially diluted mAbs were mixed in equal volume with diluted virus. Antibody-virus and virus
351 only mixtures were then incubated at 37°C with 5% CO₂ for one hour. Following incubation,
352 serially diluted mAbs and virus only controls were added in duplicate to the cells at 75 PFU at
353 37°C with 5% CO₂. After 24 hours, cells were lysed, and luciferase activity was measured via
354 Nano-Glo Luciferase Assay System (Promega) according to the manufacturer specifications.
355 Luminescence was measured by a Spectramax M3 plate reader (Molecular Devices, San Jose,
356 CA). Virus neutralization titers were defined as the sample dilution at which a 50% reduction in
357 RLU was observed relative to the average of the virus control wells.

358

359 **Surface plasmon resonance**

360 Kinetic measurements of the DH1047 Fab binding to SARS-CoV and RsSHC014 spike
361 proteins were obtained using a Biacore S200 instrument (Cytiva, formerly GE Healthcare) in
362 HBS-EP+ 1X running buffer. The spike proteins were first captured onto a Series S Streptavidin
363 chip to a level of 300-400 for the SARS-CoV spike proteins and 850-1000RU for the RsSHC014
364 spike protein. The DH1047 Fab was diluted from 2.5 to 200nM and injected over the captured
365 CoV spike proteins using the single cycle kinetics injection type at a flow rate of 50µL/min.
366 There were five 120s injections of the Fab at increasing concentrations followed by a

367 dissociation of 600s after the final injection. After dissociation, the spike proteins were
368 regenerated from the streptavidin surface using a 30s pulse of Glycine pH1.5. Results were
369 analyzed using the Biacore S200 Evaluation software (Cytiva). A blank streptavidin surface
370 along with blank buffer binding were used for double reference subtraction to account for non-
371 specific protein binding and signal drift. Subsequent curve fitting analyses were performed using
372 a 1:1 Langmuir model with a local Rmax for the DH1047 Fab. The reported binding curves are
373 representative of 2 data sets.

374

375 **Protein expression and purification for EM studies**

376 The SARS-CoV spike ectodomain construct comprised the residues 1 to 1190 (UniProt
377 P59594-1) with proline substitutions at 968-969, a C-terminal T4 fibrin trimerization motif, a
378 C-terminal HRV3C protease cleavage site, a TwinStrepTag and an 8XHisTag. The construct was
379 cloned into the mammalian expression vector p α H³⁴. The RsSHC014 spike ectodomain construct
380 was prepared similarly, except it also contained the 2P mutations that placed two consecutive
381 proline at the HR1-CH junction at residue positions 986 and 987. FreeStyle 293F cells were used
382 for the spike ectodomain production. Cells were maintained in FreeStyle 293 Expression
383 Medium (Gibco) at 37°C and 9% CO₂, with agitation at 120 rpm in a 75% humidified
384 atmosphere. Transfections were performed as previously described³⁵⁻³⁸ using Turbo293
385 (SpeedBiosystems). 16 to 18 hours post transfection, HyClone CDM4HEK293 media (Cytiva,
386 MA) was added. On the 6th day post transfection, spike ectodomain was harvested from the
387 concentrated supernatant. The purification was performed using StrepTactin resin (IBA
388 LifeSciences) and size exclusion chromatography (SEC) on a Superose 6 10/300 GL Increase
389 column (Cytiva, MA) in 2mM Tris, pH 8.0, 200 mM NaCl, 0.02% NaN₃. All steps were

390 performed at room temperature and the purified spike proteins were concentrated to 1-5 mg/ml,
391 flash frozen in liquid nitrogen and stored at -80 °C until further use.

392 DH1047 IgG was produced in Expi293F cells maintained in Expi293 Expression
393 Medium (Gibco) at 37°C, 120 rpm, 8% CO₂ and 75% humidity. Plasmids were transfected using
394 the ExpiFectamine 293 Transfection Kit and protocol (Gibco)³⁵⁻³⁷ and purified by Protein A
395 affinity. The IgG was digested to the Fab state using LysC.

396

397 **Negative Stain Electron Microscopy (NSEM)**

398 NSEM was performed as described previously¹⁶. Briefly, Fab-spike complexes were
399 prepared by mixing Fab and spike to give a 9:1 molar ratio of Fab to spike. Following a 1-hr
400 incubation for 1 hour at 37 °C, the complex was cross-linked by diluting to a final spike
401 concentration of 0.1 mg/ml into room-temperature buffer containing 150 mM NaCl, 20 mM
402 HEPES pH 7.4, 5% glycerol, and 7.5 mM glutaraldehyde and incubating for 5 minutes. Excess
403 glutaraldehyde was quenched by adding sufficient 1 M Tris pH 7.4 stock to give a final
404 concentration of 75 mM Tris and incubated for 5 minutes. Carbon-coated grids (EMS, CF300-
405 cu-UL) were glow-discharged for 20s at 15 mA, after which a 5- μ l drop of quenched sample was
406 incubated on the grid for 10-15 s, blotted, and then stained with 2% uranyl formate. After air
407 drying grids were imaged with a Philips EM420 electron microscope operated at 120 kV, at
408 82,000x magnification and images captured with a 2k x 2k CCD camera at a pixel size of 4.02 Å.

409 The RELION 3.0 program was used for all negative stain image processing. Images were
410 imported, CTF-corrected with CTFFIND, and particles were picked using a spike template from
411 previous 2D class averages of spike alone. Extracted particle stacks were subjected to 2-3 rounds
412 of 2D class averaging and selection to discard junk particles and background picks. Cleaned

413 particle stacks were then subjected to 3D classification using a starting model created from a
414 bare spike model, PDB 6vsb, low-pass filtered to 30 Å. Classes that showed clearly defined Fabs
415 were selected for final refinements followed by automatic filtering and B-factor sharpening with
416 the default Relion post-processing parameters.

417

418 **Cryo-EM**

419 Purified SARS-CoV-1 spike ectodomain was incubated for approximately 2 hours with
420 a 6-fold molar equivalent of the DH1047 Fab in a final volume of 10µL. The sample
421 concentration was adjusted to ~1.5 mg/mL of spike in 2 mM Tris pH 8.0, 200 mM NaCl, and
422 0.02% NaN₃. Before freezing, 0.1µL of glycerol was added to the 10µL of sample. A 2.4-µL
423 drop of protein was deposited on a Quantifoil-1.2/1.3 grid (Electron Microscopy Sciences, PA)
424 that had been glow discharged for 10 seconds using a PELCO easiGlow™ Glow Discharge
425 Cleaning System. After a 30-second incubation in >95% humidity, excess protein was blotted
426 away for 2.5 seconds before being plunge frozen into liquid ethane using a Leica EM GP2
427 plunge freezer (Leica Microsystems). Frozen grids were imaged using a Titan Krios (Thermo
428 Fisher) equipped with a K3 detector (Gatan). Data processing was performed using cryoSPARC
429 ³⁹. Model building and refinement was done using Phenix ^{40,41}, Coot ⁴², Pymol ⁴³, Chimera ⁴⁴,
430 ChimeraX ⁴⁵ and Isolde ⁴⁶.

431

432 **Animals and challenge viruses**

433 Eleven-month-old female BALB/c mice were purchased from Envigo (#047) and were
434 used for the SARS-CoV, SARS-CoV-2 B.1.351, and RsSHC014-CoV protection experiments. 8-
435 10-week-old hACE2-transgenic mice were bred at UNC Chapel Hill and were used for WIV-1-

436 CoV protection experiments. The study was carried out in accordance with the recommendations
437 for care and use of animals by the Office of Laboratory Animal Welfare (OLAW), National
438 Institutes of Health and the Institutional Animal Care and Use Committee (IACUC) of
439 University of North Carolina (UNC permit no. A-3410-01). Animals were housed in groups of
440 five and fed standard chow diets. Virus inoculations were performed under anesthesia and all
441 efforts were made to minimize animal suffering. All mice were anesthetized and infected
442 intranasally with 1×10^4 PFU/ml of SARS-CoV MA15, 1×10^4 PFU/ml of SARS-CoV-2
443 B1.351-MA10, 1×10^4 PFU/ml RsSHC014, 1×10^4 PFU/ml WIV-1, which have been described
444 previously^{7,22,47}. Mice were weighted daily and monitored for signs of clinical disease, and
445 selected groups were subjected to daily whole-body plethysmography. For all mouse studies,
446 groups of n=10 mice were included per arm of the study except for the hACE2-transgenic mice,
447 which included n=5 mice per group due to a limited availability of these mice. Viral titers,
448 weight loss, and histology were measured from individual mice per group.

449

450 **Lung pathology scoring**

451 Acute lung injury was quantified via two separate lung pathology scoring scales: Matute-
452 Bello and Diffuse Alveolar Damage (DAD) scoring systems. Analyses and scoring were
453 performed by a board verified veterinary pathologist who was blinded to the treatment groups as
454 described previously⁴⁸. Lung pathology slides were read and scored at 600X total magnification.

455 The lung injury scoring system used is from the American Thoracic Society (Matute-
456 Bello) in order to help quantitate histological features of ALI observed in mouse models to relate
457 this injury to human settings. In a blinded manner, three random fields of lung tissue were
458 chosen and scored for the following: (A) neutrophils in the alveolar space (none = 0, 1–5 cells =

459 1, > 5 cells = 2), (B) neutrophils in the interstitial septa (none = 0, 1–5 cells = 1, > 5 cells = 2),
460 (C) hyaline membranes (none = 0, one membrane = 1, > 1 membrane = 2), (D) Proteinaceous
461 debris in air spaces (none = 0, one instance = 1, > 1 instance = 2), (E) alveolar septal thickening
462 (< 2x mock thickness = 0, 2–4x mock thickness = 1, > 4x mock thickness = 2). To obtain a lung
463 injury score per field, A–E scores were put into the following formula score = [(20x A) + (14 x
464 B) + (7 x C) + (7 x D) + (2 x E)]/100. This formula contains multipliers that assign varying
465 levels of importance for each phenotype of the disease state. The scores for the three fields per
466 mouse were averaged to obtain a final score ranging from 0 to and including 1. The second
467 histology scoring scale to quantify acute lung injury was adopted from a lung pathology scoring
468 system from lung RSV infection in mice⁴⁹. This lung histology scoring scale measures diffuse
469 alveolar damage (DAD). Similar to the implementation of the ATS histology scoring scale, three
470 random fields of lung tissue were scored for the following in a blinded manner: 1= absence of
471 cellular sloughing and necrosis, 2=Uncommon solitary cell sloughing and necrosis (1–2
472 foci/field), 3=multifocal (3+foci) cellular sloughing and necrosis with uncommon septal wall
473 hyalinization, or 4=multifocal (>75% of field) cellular sloughing and necrosis with common
474 and/or prominent hyaline membranes. The scores for the three fields per mouse were averaged to
475 get a final DAD score per mouse. The microscope images were generated using an Olympus
476 Bx43 light microscope and CellSense Entry v3.1 software.

477

478 **Biocontainment and biosafety**

479 Studies were approved by the UNC Institutional Biosafety Committee approved by
480 animal and experimental protocols in the Baric laboratory. All work described here was
481 performed with approved standard operating procedures for SARS-CoV-2 in a biosafety level 3

482 (BSL-3) facility conforming to requirements recommended in the Microbiological and
483 Biomedical Laboratories, by the U.S. Department of Health and Human Service, the U.S. Public
484 Health Service, and the U.S. Center for Disease Control and Prevention (CDC), and the National
485 Institutes of Health (NIH).

486

487 **Statistics**

488 All statistical analyses were performed using GraphPad Prism 9.

489

490 **Data availability**

491 Structural data of DH1047 will be made available after publication.

492

493 **Code availability**

494 No code was generated in this study.

495

496 **ACKNOWLEDGEMENTS**

497 **Funding:** David R. Martinez is currently supported by a Burroughs Wellcome Fund Postdoctoral
498 Enrichment Program Award and a Hanna H. Gray Fellowship from the Howard Hugues Medical
499 Institute and was supported by an NIH NIAID T32 AI007151 and an NIAID F32 AI152296.

500 This research was also supported by funding from the Chan Zuckerberg Initiative awarded to
501 R.S.B. This project was supported by the North Carolina Policy Collaboratory at the University
502 of North Carolina at Chapel Hill with funding from the North Carolina Coronavirus Relief Fund
503 established and appropriated by the North Carolina General Assembly. This project was funded
504 in part by the National Institute of Allergy and Infectious Diseases, NIH, U.S. Department of

505 Health and Human Services award AI157155 (R.S.B), U54 CA260543 (R.S.B), AI149644
506 (R.S.B), AI145687 (P.A.), as well as an animal models contract from the NIH
507 (HHSN272201700036I). Funding was also supplied by the Intramural Research Program of the
508 Vaccine Research Center, NIAID, NIH. This work was supported by a grant from the State of
509 North Carolina with funds from the federal CARES Act, and by funds from NIH, NIAID,
510 DAIDS grant AI142596 (B.F.H). Animal histopathology services were performed by the Animal
511 Histopathology & Laboratory Medicine Core at the University of North Carolina, which is
512 supported in part by an NCI Center Core Support Grant (5P30CA016086-41) to the UNC
513 Lineberger Comprehensive Cancer Center. Part of this work was performed in the Duke
514 Regional Biocontainment Laboratory, which received partial support for construction from the
515 NIH/NIAD (UC6AI058607; G.D.S) and with support from a cooperative agreement with
516 DOD/DARPA (HR0011-17-2-0069; G.D.S). This project was also supported by the North
517 Carolina Policy Collaboratory at the University of North Carolina at Chapel Hill and Duke
518 University with funding from the North Carolina Coronavirus Relief Fund established and
519 appropriated by the North Carolina General Assembly. Cryo-EM data were collected on the
520 Titan Krios system at the Shared Materials and Instrumentation Facility in Duke University. We
521 thank Nilakshee Bhattacharya and Mark Walters for microscope alignments and assistance with
522 cryo-EM data collection. This study utilized the computational resources offered by Duke
523 Research Computing (<http://rc.duke.edu>; NIH 1S10OD018164-01) at Duke University. We thank
524 C. Kneifel, M. Newton, V. Orlikowski, T. Milledge, and D. Lane from the Duke Office of
525 Information Technology and Research Computing for assisting with setting up and maintaining
526 the computing environment. We thank A. Foulger, N. Jamieson, J. Kittrell, E. Lee, and A.
527 Sanzone for DNA and antibody production.

528

529 **Author contributions:** Conceived the study: D.R.M., A.S., S.G., D.L., P.A., B.F.H., R.S.B.
530 designed experiments: D.R.M., A.S., S.G., D.L., performed laboratory experiments: D.R.M.,
531 A.S., D.L., S.G., Provided critical reagents: T.Z., P.D.K., B.S.G., and K.O.S. Analyzed data and
532 provided critical insight: D.R.M, A.S., S.G., D.L., G.D.LC., R.P., M.B., K.M., B.Y., K.A., S.M.,
533 T.Z., P.D.K., B.S.G., J.R.M., D.C.M, M.A., G.D.S., K.W., K.O.S., P.A., B.F.H., R.S.B.; Wrote
534 the first draft of the paper: D.R.M; Read and edited the paper: D.R.M, A.S., S.G., D.L., T.Z.,
535 P.D.K., B.S.G., J.R.M., D.C.M, M.A., G.D.S., K.W., K.O.S., P.A., B.F.H., R.S.B. Funding
536 acquisition: D.R.M., G.D.S., B.F.H., R.S.B. All authors reviewed and approved the manuscript.
537 **Competing interests:** Duke University has filed provisional patents for which B.F.H, K.O.S.,
538 D.L., and G.D.S., are inventors on a provisional U.S. patent for mAb DH1047 and its
539 applications described in this study.

540

541

542

543

544

545

546

547

548

549

550

551

552 **REFERENCES**

- 553 1. Peiris, J.S., *et al.* Coronavirus as a possible cause of severe acute respiratory syndrome.
554 *Lancet* **361**, 1319-1325 (2003).
- 555 2. Cherry, J.D. & Krogstad, P. SARS: The First Pandemic of the 21st Century. *Pediatric*
556 *Research* **56**, 1-5 (2004).
- 557 3. Zaki, A.M., van Boheemen, S., Bestebroer, T.M., Osterhaus, A.D. & Fouchier, R.A.
558 Isolation of a novel coronavirus from a man with pneumonia in Saudi Arabia. *N Engl J*
559 *Med* **367**, 1814-1820 (2012).
- 560 4. Zhou, P., *et al.* A pneumonia outbreak associated with a new coronavirus of probable bat
561 origin. *Nature* **579**, 270-273 (2020).
- 562 5. Li, W., *et al.* Bats Are Natural Reservoirs of SARS-Like Coronaviruses. *Science* **310**,
563 676-679 (2005).
- 564 6. Hu, B., *et al.* Discovery of a rich gene pool of bat SARS-related coronaviruses provides
565 new insights into the origin of SARS coronavirus. *PLoS Pathog* **13**, e1006698 (2017).
- 566 7. Menachery, V.D., *et al.* A SARS-like cluster of circulating bat coronaviruses shows
567 potential for human emergence. *Nat Med* **21**, 1508-1513 (2015).
- 568 8. Menachery, V.D., *et al.* SARS-like WIV1-CoV poised for human emergence. *Proc Natl*
569 *Acad Sci U S A* **113**, 3048-3053 (2016).
- 570 9. Martinez, D.R., *et al.* Chimeric spike mRNA vaccines protect against sarbecovirus
571 challenge in mice. *bioRxiv*, 2021.2003.2011.434872 (2021).
- 572 10. Saunders, K.O., *et al.* SARS-CoV-2 vaccination induces neutralizing antibodies against
573 pandemic and pre-emergent SARS-related coronaviruses in monkeys. *bioRxiv* (2021).
- 574 11. Walls, A.C., *et al.* Elicitation of broadly protective sarbecovirus immunity by receptor-
575 binding domain nanoparticle vaccines. *bioRxiv* (2021).
- 576 12. Wang, L., *et al.* Antibodies with potent and broad neutralizing activity against
577 antigenically diverse and highly transmissible SARS-CoV-2 variants. *bioRxiv* (2021).
- 578 13. Wang, P., *et al.* Antibody resistance of SARS-CoV-2 variants B.1.351 and B.1.1.7.
579 *Nature* (2021).
- 580 14. Chen, R.E., *et al.* Resistance of SARS-CoV-2 variants to neutralization by monoclonal
581 and serum-derived polyclonal antibodies. *Nat Med* (2021).
- 582 15. Rappazzo, C.G., *et al.* Broad and potent activity against SARS-like viruses by an
583 engineered human monoclonal antibody. *Science* **371**, 823-829 (2021).
- 584 16. Li, D., *et al.* The functions of SARS-CoV-2 neutralizing and infection-enhancing
585 antibodies in vitro and in mice and nonhuman primates. *bioRxiv* (2021).
- 586 17. Whittle, J.R., *et al.* Broadly neutralizing human antibody that recognizes the receptor-
587 binding pocket of influenza virus hemagglutinin. *Proc Natl Acad Sci U S A* **108**, 14216-
588 14221 (2011).
- 589 18. An EUA for Bamlanivimab—A Monoclonal Antibody for COVID-19. *JAMA* (2020).
- 590 19. Martinez, D.R., *et al.* Prevention and therapy of SARS-CoV-2 and the B.1.351 variant in
591 mice. *bioRxiv*, 2021.2001.2027.428478 (2021).
- 592 20. Leist, S.R., Schäfer, A. & Martinez, D.R. Cell and animal models of SARS-CoV-2
593 pathogenesis and immunity. *Dis Model Mech* **13**(2020).

- 594 21. Planas, D., *et al.* Sensitivity of infectious SARS-CoV-2 B.1.1.7 and B.1.351 variants to
595 neutralizing antibodies. *Nature Medicine* (2021).
- 596 22. Leist, S.R., *et al.* A Mouse-Adapted SARS-CoV-2 Induces Acute Lung Injury and
597 Mortality in Standard Laboratory Mice. *Cell* **183**, 1070-1085.e1012 (2020).
- 598 23. Davies, N.G., *et al.* Estimated transmissibility and impact of SARS-CoV-2 lineage
599 B.1.1.7 in England. *Science* **372**, eabg3055 (2021).
- 600 24. Davies, N.G., *et al.* Increased mortality in community-tested cases of SARS-CoV-2
601 lineage B.1.1.7. *Nature* (2021).
- 602 25. Sadoff, J., *et al.* Safety and Efficacy of Single-Dose Ad26.COV2.S Vaccine against
603 Covid-19. *New England Journal of Medicine* (2021).
- 604 26. Madhi, S.A., *et al.* Efficacy of the ChAdOx1 nCoV-19 Covid-19 Vaccine against the
605 B.1.351 Variant. *New England Journal of Medicine* (2021).
- 606 27. Wang, Z., *et al.* mRNA vaccine-elicited antibodies to SARS-CoV-2 and circulating
607 variants. *Nature* (2021).
- 608 28. Wang, C., *et al.* A conserved immunogenic and vulnerable site on the coronavirus spike
609 protein delineated by cross-reactive monoclonal antibodies. *Nature Communications* **12**,
610 1715 (2021).
- 611 29. Zhou, P., *et al.* A protective broadly cross-reactive human antibody defines a conserved
612 site of vulnerability on beta-coronavirus spikes. *bioRxiv* (2021).
- 613 30. Sauer, M.M., *et al.* Structural basis for broad coronavirus neutralization. *bioRxiv* (2020).
- 614 31. Jennewein, M.F., *et al.* Isolation and Characterization of Cross-Neutralizing Coronavirus
615 Antibodies from COVID-19+ Subjects. *bioRxiv* (2021).
- 616 32. Tortorici, M.A., *et al.* Structural basis for broad sarbecovirus neutralization by a human
617 monoclonal antibody. *bioRxiv* (2021).
- 618 33. Jette, C.A., *et al.* Broad cross-reactivity across sarbecoviruses exhibited by a subset of
619 COVID-19 donor-derived neutralizing antibodies. *bioRxiv*, 2021.2004.2023.441195
620 (2021).
- 621 34. Wrapp, D., *et al.* Cryo-EM structure of the 2019-nCoV spike in the prefusion
622 conformation. *Science* **367**, 1260-1263 (2020).
- 623 35. Henderson, R., *et al.* Controlling the SARS-CoV-2 spike glycoprotein conformation. *Nat*
624 *Struct Mol Biol* (2020).
- 625 36. Li, D., *et al.* The functions of SARS-CoV-2 neutralizing and infection-enhancing
626 antibodies in vitro and in mice and nonhuman primates. *bioRxiv* (2021).
- 627 37. Acharya, P., *et al.* A glycan cluster on the SARS-CoV-2 spike ectodomain is recognized
628 by Fab-dimerized glycan-reactive antibodies. *bioRxiv* (2020).
- 629 38. Edwards, R.J., *et al.* Cold sensitivity of the SARS-CoV-2 spike ectodomain. *Nature*
630 *Structural & Molecular Biology* **28**, 128-131 (2021).
- 631 39. Punjani, A., Rubinstein, J.L., Fleet, D.J. & Brubaker, M.A. cryoSPARC: algorithms for
632 rapid unsupervised cryo-EM structure determination. *Nature Methods* **14**, 290-296
633 (2017).
- 634 40. Liebschner, D., *et al.* Macromolecular structure determination using X-rays, neutrons and
635 electrons: recent developments in Phenix. *Acta Crystallographica Section D Structural*
636 *Biology* **75**, 861-877 (2019).
- 637 41. Afonine, P.V., *et al.* Real-space refinement in PHENIX for cryo-EM and crystallography.
638 *Acta Crystallographica Section D Structural Biology* **74**, 531-544 (2018).

- 639 42. Emsley, P., Lohkamp, B., Scott, W.G. & Cowtan, K. Features and development of Coot.
640 *Acta Crystallographica Section D Biological Crystallography* **66**, 486-501 (2010).
641 43. Schrodinger, L. The PyMOL Molecular Graphics System. (2015).
642 44. Pettersen, E.F., *et al.* UCSF Chimera?A visualization system for exploratory research and
643 analysis. *Journal of Computational Chemistry* **25**, 1605-1612 (2004).
644 45. Goddard, T.D., *et al.* UCSF ChimeraX: Meeting modern challenges in visualization and
645 analysis. *Protein Science* **27**, 14-25 (2018).
646 46. Croll, T.I. ISOLDE: a physically realistic environment for model building into low-
647 resolution electron-density maps. *Acta Crystallogr D Struct Biol* **74**, 519-530 (2018).
648 47. Roberts, A., *et al.* A mouse-adapted SARS-coronavirus causes disease and mortality in
649 BALB/c mice. *PLoS Pathog* **3**, e5 (2007).
650 48. Sheahan, T.P., *et al.* Comparative therapeutic efficacy of remdesivir and combination
651 lopinavir, ritonavir, and interferon beta against MERS-CoV. *Nature Communications* **11**,
652 222 (2020).
653 49. Schmidt, M.E., *et al.* Memory CD8 T cells mediate severe immunopathology following
654 respiratory syncytial virus infection. *PLoS Pathog* **14**, e1006810 (2018).
655

656

657

658

659

660

661

662

663

664

665

666

667

668

669

670

671

672 **Figure legends**

673 **Figure 1. The identification of cross-reactive and broadly neutralizing antibodies.**

674 The neutralization activity of four broadly neutralizing antibodies against SARS-CoV-2 2AA
675 mouse-adapted (MA), SARS-CoV, WIV-1, and RsSHC014. SARS-CoV-2 2AA MA is shown in
676 purple, SARS-CoV is shown in orange, WIV-1 is shown in pink, and RsSHC014 is shown in
677 green. The neutralization activity against Sarbecoviruses is shown for (A) DH1235, (B) DH1073,
678 (C) DH1046, and (D) DH1047. The binding activity of cross-reactive antibodies against SARS-
679 CoV spike, SARS-CoV-2 spike, SARS-CoV-2 RBD, Pangolin GXP4L spike, RaTG13 spike,
680 and RsSHC014 spike of (E) DH1235, (F) DH1073, (G) DH1046, and (H) DH1047.

681

682 **Figure 2: Prevention and therapy of DH1047 against SARS-CoV in aged mice.**

683 (A) SARS-CoV mouse-adapted 15 (MA15) lung viral replication in the prophylactically treated
684 (-12 hours before infection) mice with a control influenza mAb CH65 and the four broadly
685 neutralizing antibodies DH1235, DH1073, DH1046, DH1047.

686 (B) % Starting weight of prophylactic (-12 hours before infection) and therapeutic (+12 hours
687 after infection) treatment with DH1047 and control against SARS-CoV MA15 in mice.

688 (C) Lung viral replication of SARS-CoV MA15 in mice treated prophylactically and
689 therapeutically with DH1047 and control at 4 days post infection.

690 (D) Macroscopic lung discoloration scores in mice treated with DH1047 and control
691 prophylactically and therapeutically.

692 (E) Lung pathology at day 4 post infection measured by acute lung injury (ALI) scores in mice
693 treated with DH1047 and control prophylactically and therapeutically.
694 (F) Lung pathology at day 4 post infection measured by diffuse alveolar damage (DAD) in mice
695 treated prophylactically and therapeutically with DH1047 and control.
696 (G) Pulmonary function as measured by whole body plethysmography (Buxco) in DH1047 and
697 control mAb prophylactically and therapeutically treated mice. P values are from a 2-way
698 ANOVA after Tukey's multiple comparisons test for the weight loss, and P values are from a 1-
699 way ANOVA following Dunnett's multiple comparisons for the viral titer, and lung pathology
700 readouts.

701

702 **Figure 3. Cryo-EM structure of DH1047 bound to SARS-CoV spike.**

703 (A) Cryo-EM reconstruction of DH1047 Fab bound to SARS-CoV spike shown in grey, with the
704 underlying fitted model shown in cartoon representation. DH1047 is colored green, the RBD it is
705 bound to is colored black with the Receptor Binding Motif within the RBD colored purple.
706 (B) Overlay of DH1047 bound to SARS-CoV-1 and SARS-CoV-2 (PDB ID: 7LDI) S proteins.
707 Overlay was performed with the respective RBDs. DH1047 bound to SARS-CoV and SARS-
708 CoV-2 spike is shown in green and salmon, respectively.
709 (C) ACE2 (yellow surface representation, PDB 6VW1) binding to RBD is sterically hindered by
710 DH1047. The views in panels B and C are related by a $\sim 180^\circ$ rotation about the vertical axis.
711 (D) DH1047 binding relative to binding of other known antibody classes that bind the RBD.
712 RBD is shown in black with the ACE2 footprint on the RBD colored yellow. DH1047 is shown
713 in cartoon representation and colored green. The other antibodies are shown as transparent
714 surfaces: C105 (pale cyan, Class 1, PDB ID: 6XCN and 6XCA), DH1041 (light blue, Class 2,

715 PDB ID: 7LAA), S309 (wheat, Class 3, PDB ID:6WS6 and 6WPT) and CR3022 (pink, Class 4 ,

716 PDB ID: 6YLA)

717

718 **Figure 4: Prophylactic and therapeutic activity of DH1047 against SARS-like bat CoVs and**
719 **the *in vitro* neutralization against the SARS-CoV-2 variants.**

720 (A) Lung viral replication of WIV-1 in mice treated prophylactically and therapeutically with
721 DH1047 and control at 2 days post infection.

722 (B) Lung viral replication of RsSHC014 in mice treated prophylactically and therapeutically with
723 DH1047 and control at 2 days post infection.

724 (C) Live virus neutralization of SARS-CoV-2 D614G, UK B.1.1.7., and South African B.1.351
725 variants.

726 (D) The comparison of the DH1047 neutralization activity against the SARS-CoV-2 variants in
727 pseudovirus and live virus neutralization assays. P values are from a 2-way ANOVA after
728 Tukey's multiple comparisons test for the weight loss, and P values are from a 1-way ANOVA
729 following Dunnett's multiple comparisons for the viral titer, and lung pathology readouts.

730

731

732 **Figure 5: Prevention and therapy of DH1047 against SARS-CoV-2 B.1.351 in mice.**

733 (A) % Starting weight of prophylactic (-12 hours before infection) and therapeutic (+12 hours
734 after infection) treatment with DH1047 and control against SARS-CoV-2 B.1.351 in mice.

735 (B) Lung viral replication of SARS-CoV-2 B.1.351 in mice treated prophylactically and
736 therapeutically with DH1047 and control at 4 days post infection.

737 (C) Macroscopic lung discoloration scores in mice treated with DH1047 and control
738 prophylactically and therapeutically.
739 (E) Lung pathology at day 4 post infection measured by acute lung injury (ALI) scores in mice
740 treated with DH1047 and control prophylactically and therapeutically.
741 (F) Lung pathology at day 4 post infection measured by diffuse alveolar damage (DAD) in mice
742 treated prophylactically and therapeutically with DH1047 and control. P values are from a 2-way
743 ANOVA after Tukey's multiple comparisons test for the weight loss, and P values are from a 1-
744 way ANOVA following Dunnett's multiple comparisons for the viral titer, and lung pathology
745 readouts.

746

747

748 **Supplemental Figure Legends**

749

750 **Figure S1. The binding activity of cross-reactive antibodies against MERS-CoV and human**
751 **common-cold CoVs.**

752 The neutralization activity of four broadly neutralizing antibodies against SARS-CoV-2 NTD,
753 MERS-CoV spike, HCoV-OC43 spike, HCoV-NL63, and HCoV-229E shown for (A) DH1235,
754 (B) DH1073, (C) DH1046, and (D) DH1047.

755

756 **Figure S2. NSEM of DH1047 bound to bat RsSHC014 and SARS-CoV spike ectodomains.**

757 (A) Representative 2D class averages of bat RsSHC014 2P spike ectodomain bound to DH1047
758 Fab.

759 (B) Overlay of 3D reconstruction of DH1047 bound to bat RsSHC014 2P (grey) and SARS-
760 CoV-2 HexaPro (purple) S ectodomains.
761 (C) Representative 2D class averages of SARS-CoV 2P spike ectodomain bound to DH1047 Fab
762 (D) Overlay of 3D reconstruction of DH1047 bound to bat SARS-CoV 2P (grey) and SARS-
763 CoV-2 HexaPro (purple) S ectodomains. The red boxes in panels A and C indicate the classes
764 that show DH1047 Fab bound to spike.

765

766

767 **Figure S3. Lung H+E staining of SARS-CoV infected mice.**

768 Pathologic features of acute lung injury were scored using two separate tools: the American
769 Thoracic Society Lung Injury Scoring (ATS ALI) system. Using this ATS ALI system, we
770 created an aggregate score for the following features: neutrophils in the alveolar and interstitial
771 space, hyaline membranes, proteinaceous debris filling the air spaces, and alveolar septal
772 thickening. Three randomly chosen high power ($\times 60$) fields of diseased lung were assessed per
773 mouse. Representative images are shown from vehicle and RDV-treated mice. All images were
774 taken at the same magnification. The black bar indicates 100 μm scale. (A) CH65 control
775 prophylaxis. (B) CH65 therapy. (C) DH1047 prophylaxis. (D) DH1047 therapy.

776

777

778 **Figure S4. The affinity data of DH1047 against SARS-CoV and RsSHC014 spikes.**

779 Surface plasmon resonance (SPR) binding experiments of DH1047 against (A) SARS-CoV-2
780 Toronto and (B) RsSHC014. Binding affinity measurements are shown in the tables and response

781 units (RU) as a function of time in seconds (s) is shown for both SARS-CoV and RsSHC014.

782 SPR experiments were repeated twice.

783

784 **Figure S5. Cryo-EM data processing for the SARS-CoV spike ectodomain bound to**

785 **DH1047, Related to Figure 2.**

786 (A) Representative cryo-EM micrograph.

787 (B) Cryo-EM CTF fit.

788 (C) Representative 2D class averages from Cryo-EM dataset.

789 (D) *Ab initio* reconstruction.

790 (E) Refined map.

791 (F) Fourier shell correlation curve.

792 (G) Refined cryo-EM map colored by local resolution.

793 (H) Zoom-in images showing the SD1, NTD, HR1/CH and RBD/Fab contact regions in the

794 structure. The cryo-EM map is shown as a blue mesh and the fitted model is in cartoon

795 representation, with residues shown as stick.

796

797 **Figure S6. DH1047 and ADG-2 binds the RBD of SARS-Cov and SARS-CoV-2 spike**

798 **ectodomains using a similar footprint.**

799 (A) Cartoon representation of DH1047 (colored in pale green) bound to the RBD (grey surface,

800 ACE2 binding site in yellow) of SARS-CoV S ectodomain and ADG-2 (cyan) bound to SARS-

801 CoV-2 S ectodomain. The homologous Fab ADI-19425 (PDB 6APC) was docked in the ADG-2

802 cryo-EM map (EMD-23160) to generate the model.

803 (B) DH1047 and ADG-2 bind partially overlapping binding sites on the RBD.

804

805 **Supplemental Table 1: monoclonal antibody screen against SARS-CoV-2 2AA MA, SARS-**
806 **CoV, WIV-1, and RsSHC014**

807

808 **Supplemental Table 2: Immunogenetic characteristics of broadly cross-reactive mAbs.**

809

810

811

812

813

814

815

816

817

818

819

820

821

822

823

824

825

826

827

PDB ID	828	Supplementary Table 3.
EMDB ID	829	Cryo-EM data collection and
Data collection and processing		
Microscope	FEI Titan Krios ⁸³⁰	refinements statistics.
Detector	Gatan K3	
Magnification	81,000	
Voltage (kV)	300	
Electron exposure (e ⁻ /Å ²)	54.1	
Defocus range (µm)	~0.75-2.50	
Pixel size (Å)	1.08	
Reconstruction software	cryoSparc	
Symmetry imposed	C1	
Initial particle images (no.)	2,370,616	
Final particle images (no.)	284,619	
Map resolution (Å)	3.43	
FSC threshold	0.143	
Refinement		
Initial model used	7LD1	
Model resolution (Å)	3.43	
FSC threshold	0.143	
Model composition		
Nonhydrogen atoms	28,048	
Protein residues	3,737	
R.m.s. deviations		
Bond lengths (Å)	0.016	
Bond angles (°)	1.956	
Validation		
MolProbity score	1.79	
Clashscore	1.65	
Poor rotamers (%)	2.36	

EM ringer score	2.9	831
Ramachandran plot		
Favored (%)	88.54	832
Allowed (%)	9.79	833
Disallowed (%)	1.66	
<hr/>		834

835

Figure 1

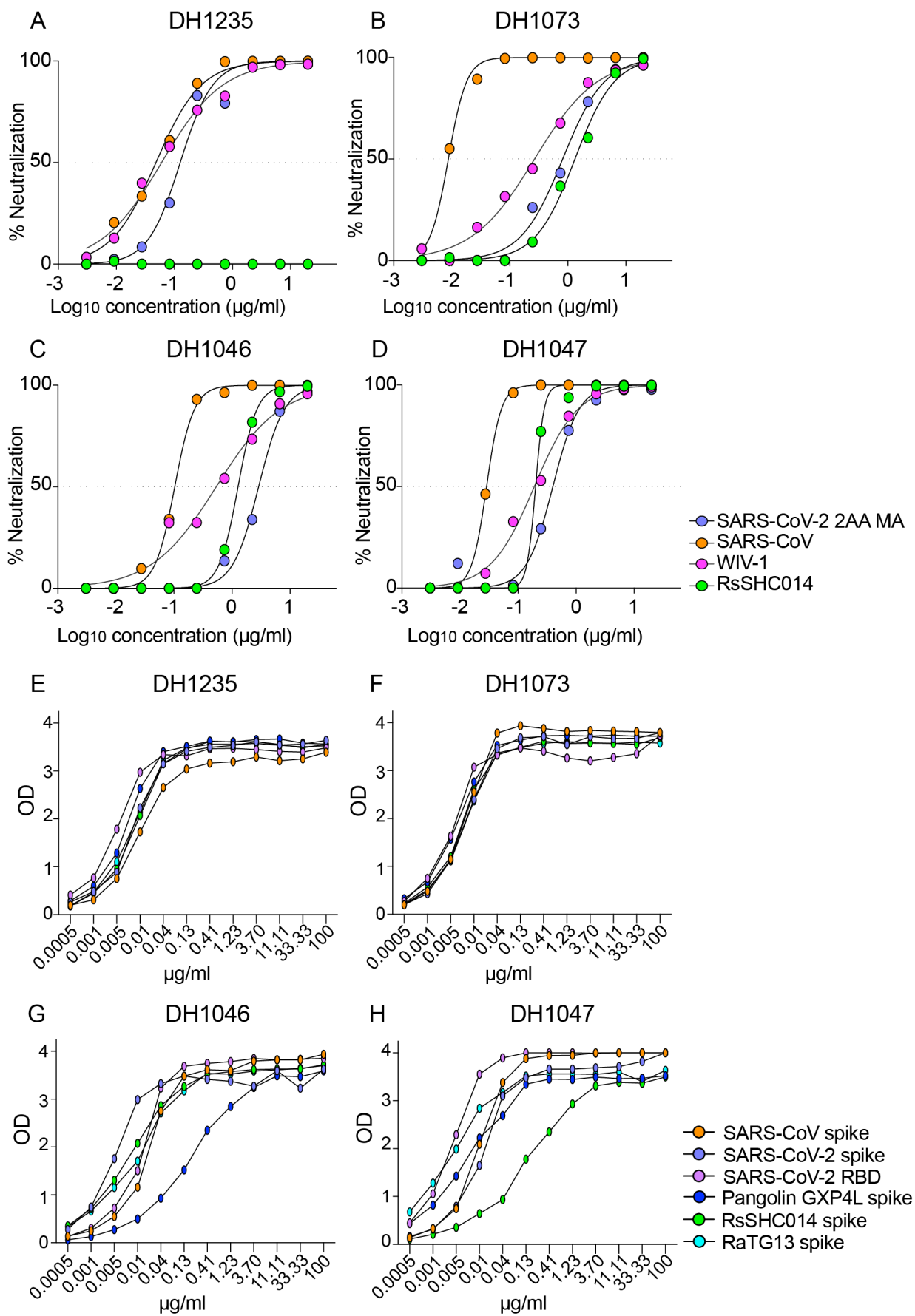


Figure 2

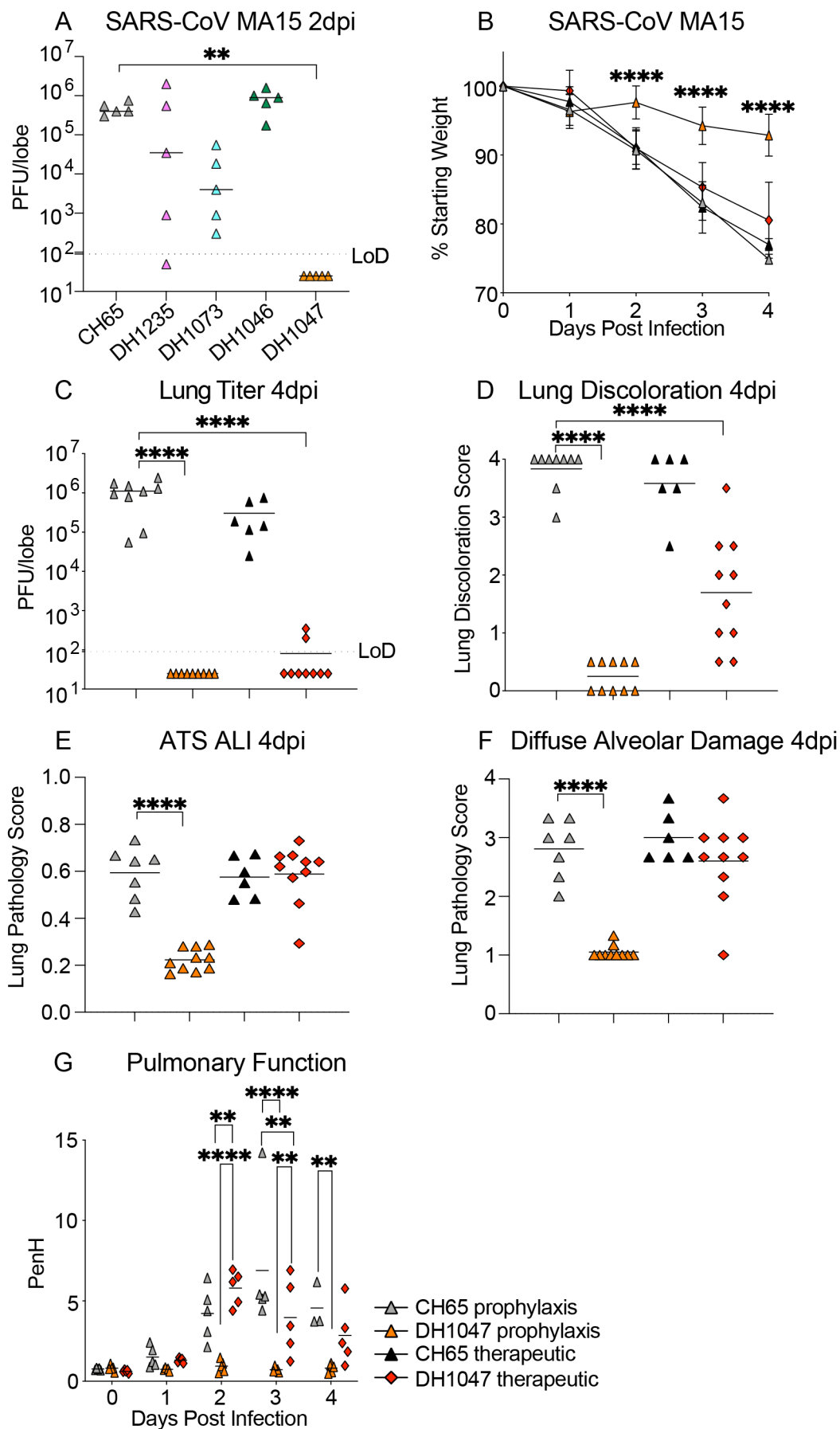


Figure 3

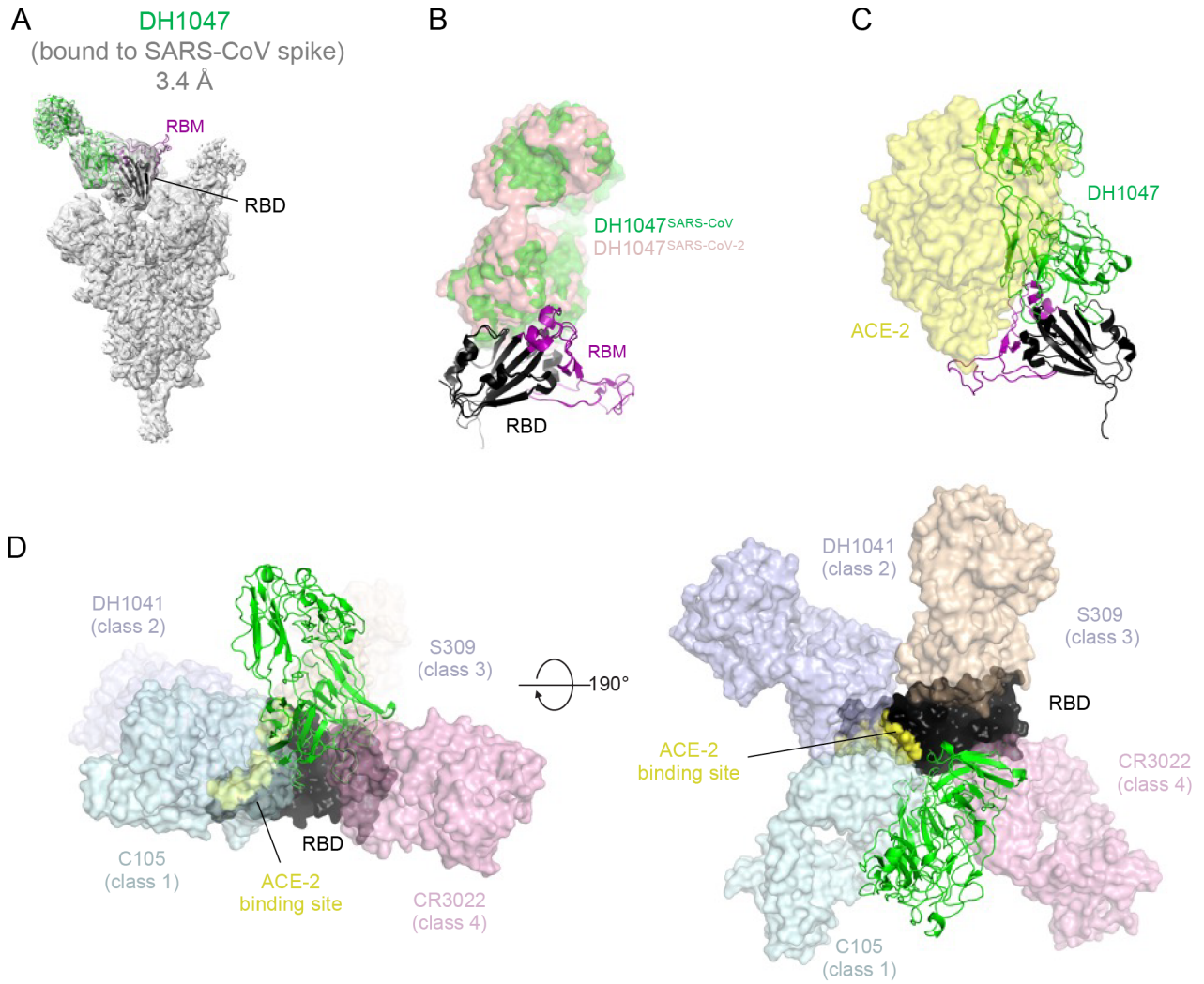
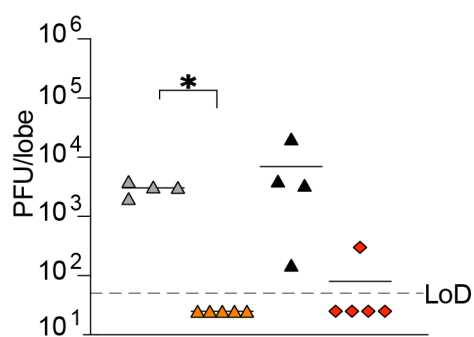
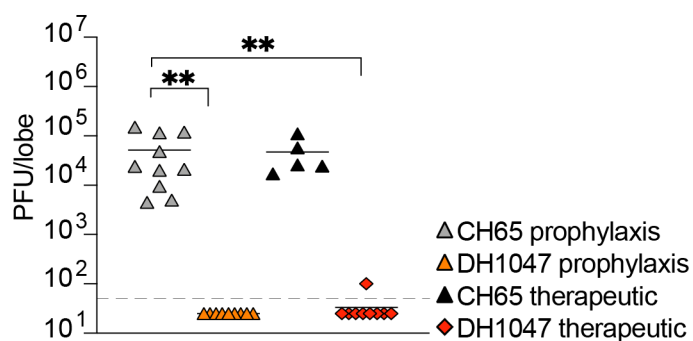


Figure 4

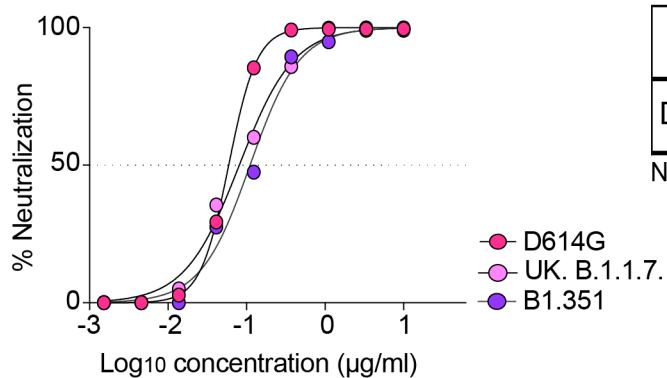
A WIV-1-CoV Titer 2dpi



B RsSHC014-CoV Titer 2dpi



C Live SARS-CoV-2 virus



D

mAb	Assay	D614G	B.1.1.7.	B1.429	B1.351
		IC ₅₀ (µg/ml)			
DH1047	pseudovirus	0.181	0.223	0.220	0.266
	live virus	0.059	0.081	NT	0.111

NT: not tested

Figure 5

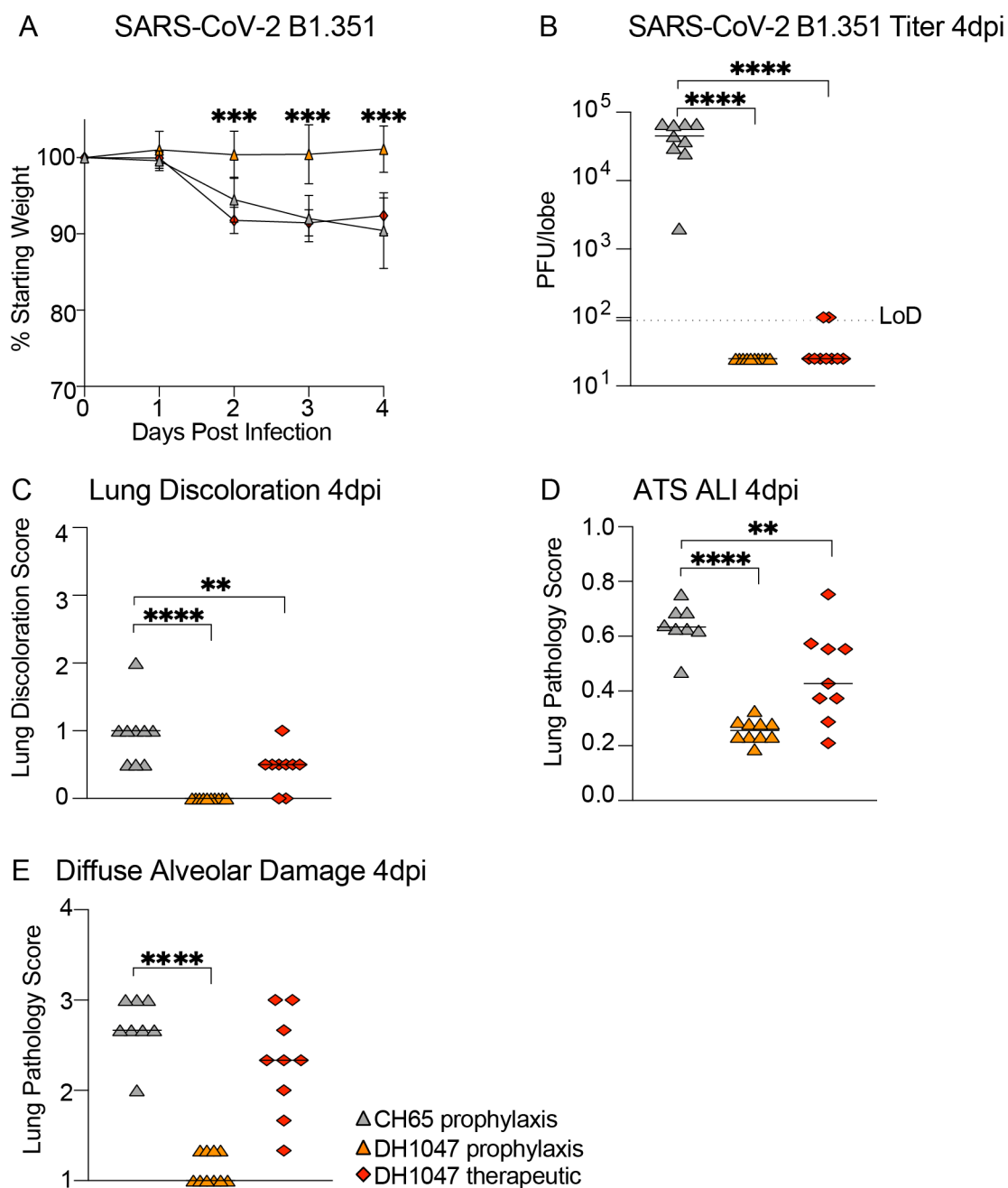


Figure S1

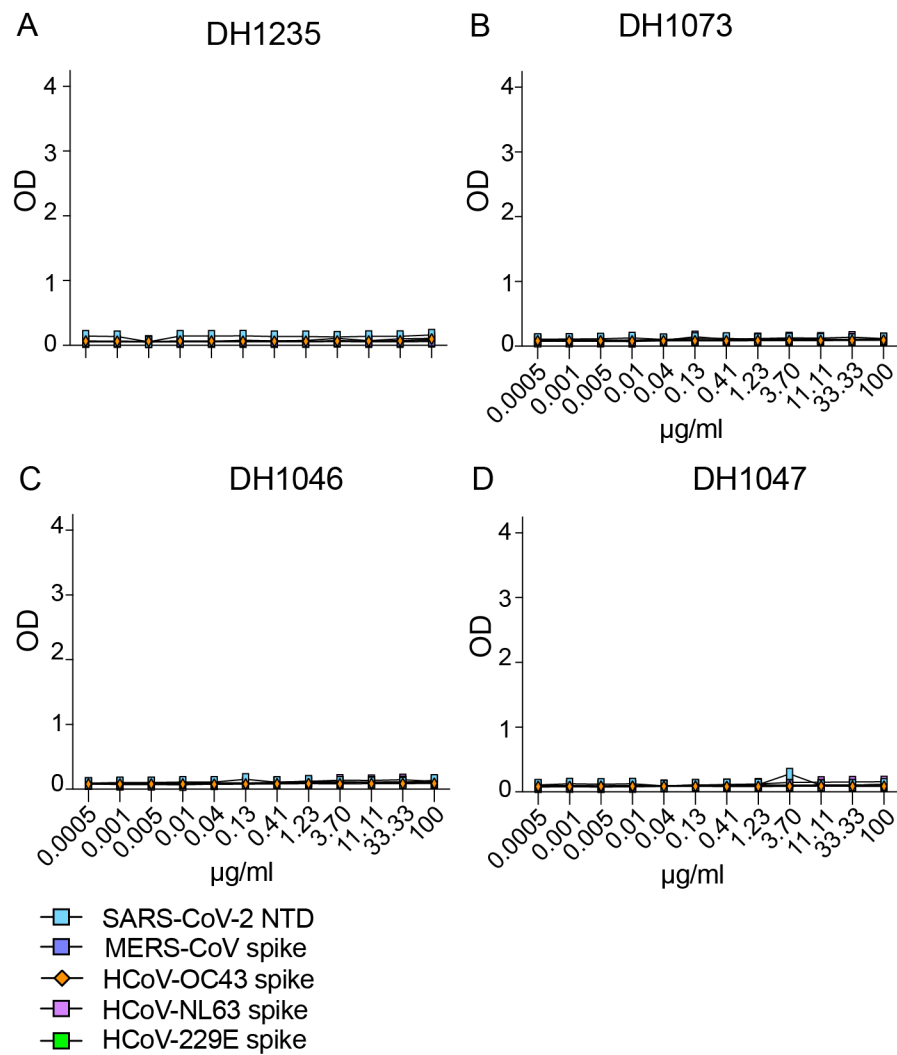
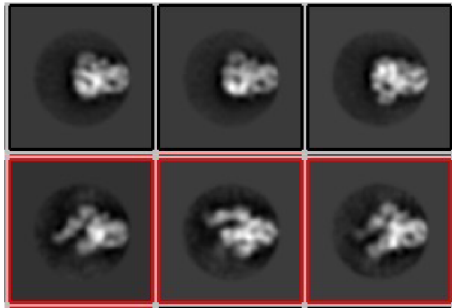
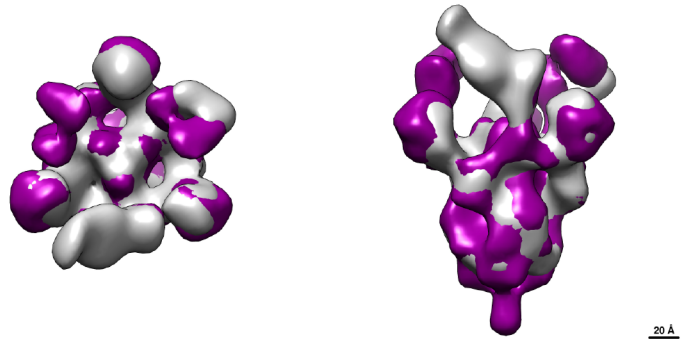


Figure S2

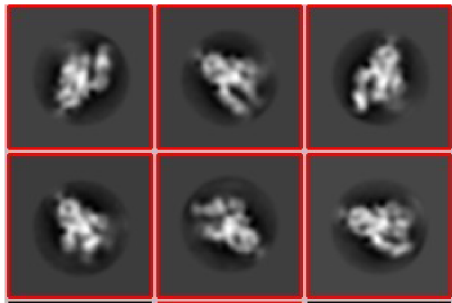
A



B



C



D

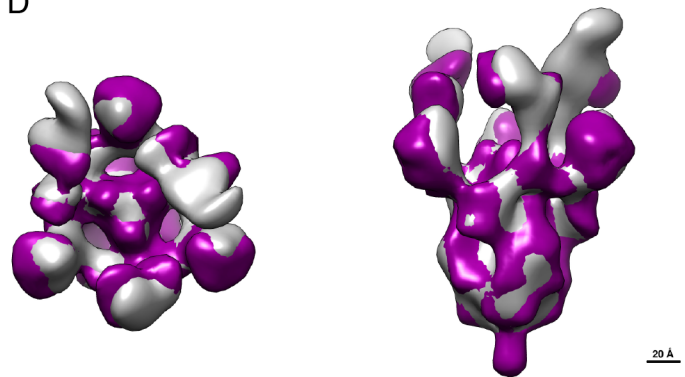
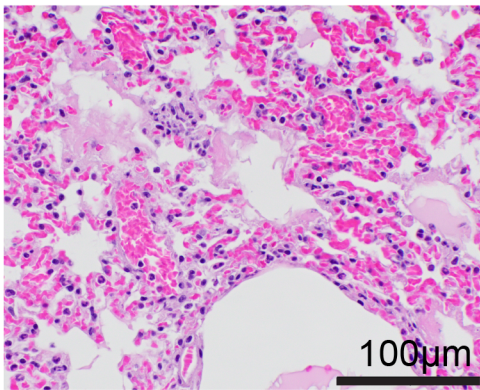
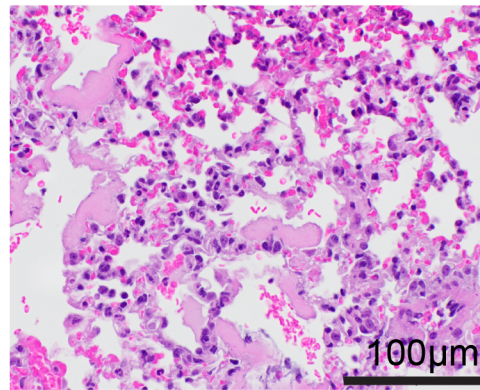


Figure S3

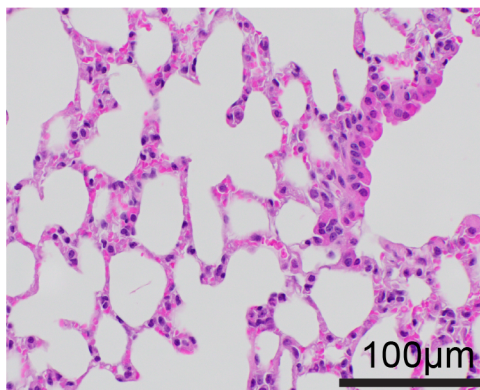
A CH65 control -12hr prophylaxis



B CH65 +12hr therapy



C DH1047 -12hr prophylaxis



D DH1047 +12hr therapy

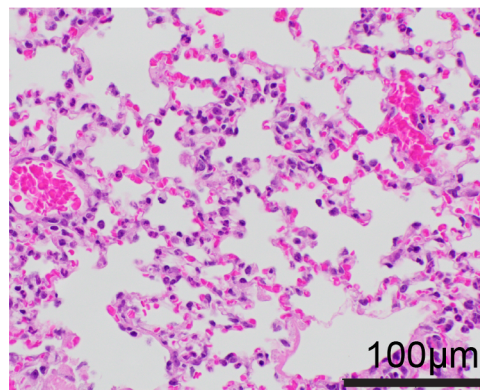
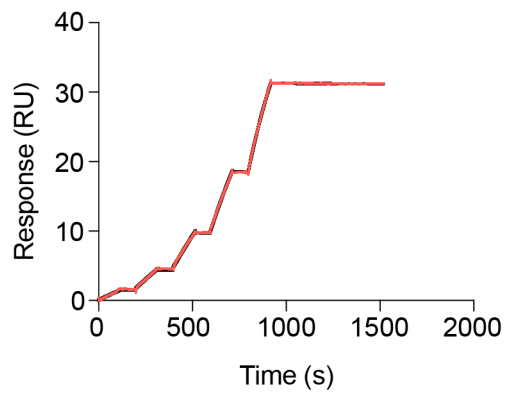


Figure S4

A

SARS-CoV Toronto spike			
Fab	ka (1/Ms)	kd (1/s)	KD(nM)
DH1047	9.622E+4	<1.0E-5	<0.1

DH1047 Fab vs. SARS-CoV Toronto



B

RsSCH014 spike			
Fab	ka (1/Ms)	kd (1/s)	KD(nM)
DH1047	8.602E+4	<1.0E-5	<0.1

DH1047 Fab vs. RsSHc014

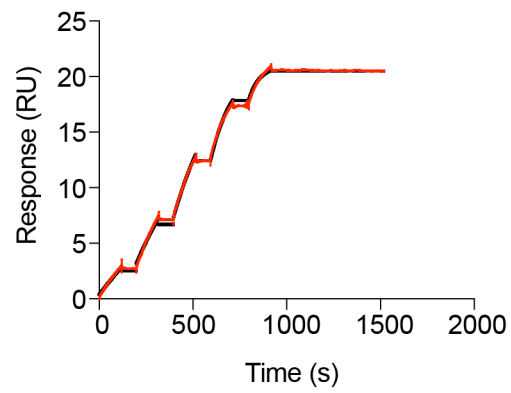


Figure S5

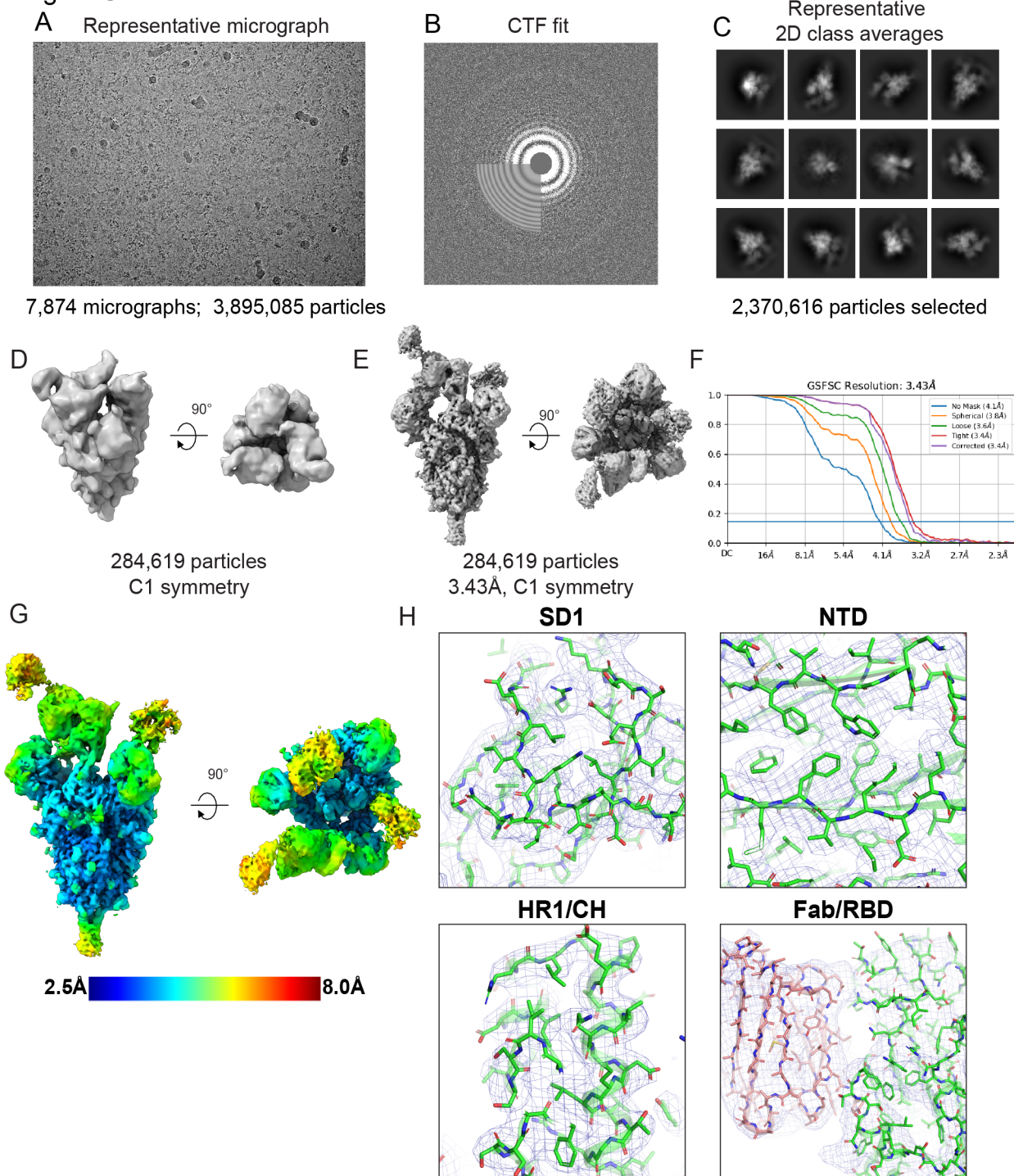
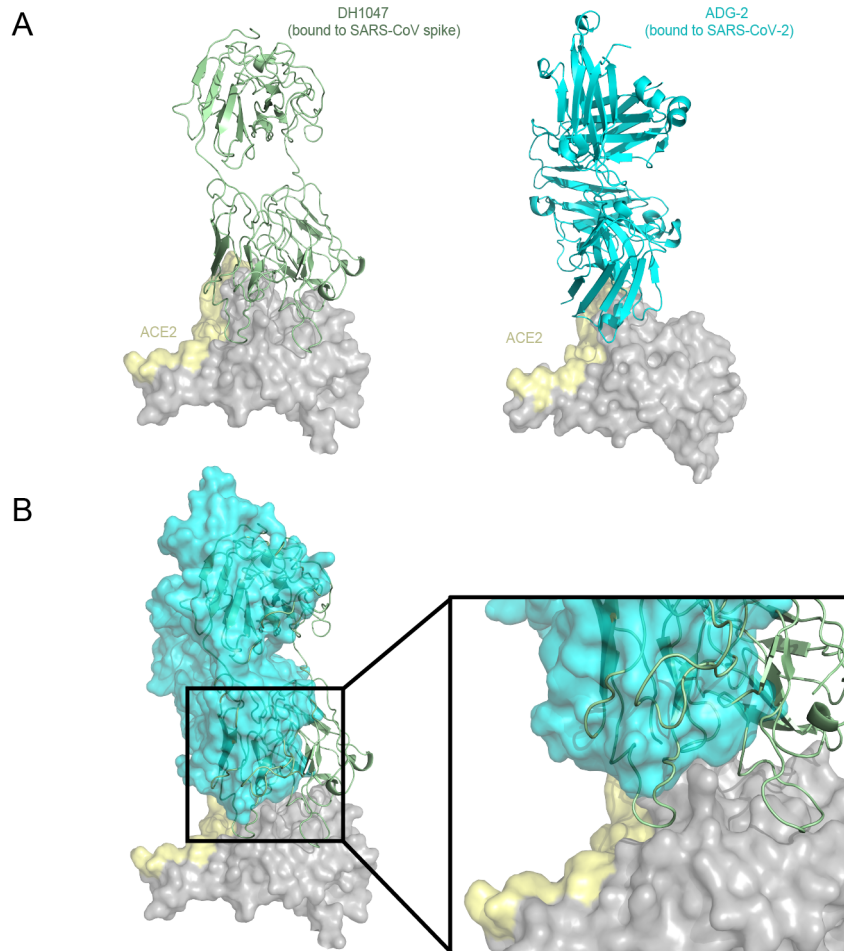


Figure S6



Supplemental Table 1: monoclonal antibody screen against SARS-CoV-2 2AA MA, SARS-CoV, WIV-1, and RsSHC014

mAb #	DH #	mAb	Specificity to SARS-CoV-2	ELISA cross-reactivity	Live virus neutralization IC ₅₀ (µg/ml)			
					SARS-CoV-2 2AA MA	SARS-CoV	WIV-1	RsSHC014
1	DH1058	Ab711725_G1.4A/293i/Citrate	S2	SARS-CoV-1, MERS-CoV, 229E, NL63, HKU1, OC43	>10	>10	>10	>10
2	DH1057	Ab025934_G1.4A/293i/Citrate	S2	SARS-CoV-1, OC43	>10	>10	>10	>10
18	DH1047	Ab712384_LS/293i/Citrate	RBD	SARS-CoV, SARS-CoV-2, and bat CoVs	0.3979	0.0287	0.191	0.2005
45	DH1203	Ab026044_LS/293i/Citrate	RBD	SARS-CoV and SARS-CoV-2	3.768	0.04781	>10	>10
46	DH1127	Ab026075_LS/293i/Citrate	RBD	SARS-CoV and SARS-CoV-2	>10	>10	>10	>10
47	DH1059	Ab026129L2_LS/293i/Citrate	no binding	SARS-CoV-2	>10	>10	>10	>10
48	DH1081	Ab026147_LS/293i/Citrate	NTD	SARS-CoV and SARS-CoV-2	>10	>10	>10	>10
49	DH1085	Ab026160_LS/293i/Citrate	no binding	SARS-CoV-2	>10	>10	>10	>10
50	DH1080	Ab026162_LS/293i/Citrate	RBD	SARS-CoV and SARS-CoV-2	>10	0.0059	0.0330	>10
51	DH1061.1	Ab026164_LS/293i/Citrate	NTD	SARS-CoV and SARS-CoV-2	>10	>10	>10	>10
52	DH1065	Ab026172_LS/293i/Citrate	NTD	SARS-CoV and SARS-CoV-2	>10	>10	>10	>10
53	DH1066	Ab026186_LS/293i/Citrate	NTD	only SARS-CoV	>10	>10	>10	>10
54	DH1064	Ab026188_LS/293i/Citrate	RBD	SARS-CoV and SARS-CoV-2	>10	0.0216	>10	>10
55	DH1067	Ab026196_LS/293i/Citrate	NTD	SARS-CoV and SARS-CoV-2	>10	>10	>10	>10
56	DH1069	Ab026200_LS/293i/Citrate	NTD	SARS-CoV and SARS-CoV-2	>10	>10	>10	>10
57	DH1046	Ab026204_LS/293i/Citrate	RBD	SARS-CoV, SARS-CoV-2, and bat CoVs	2.857	0.1033	0.4248	1.274
58	DH1068	Ab026217_LS/293i/Citrate	NTD	SARS-CoV and SARS-CoV-2	>10	>10	>10	>10
59	DH1086	Ab026240_LS/293i/Citrate	NTD	SARS-CoV and SARS-CoV-2	>10	>10	>10	>10
60	DH1071	Ab026243_LS/293i/Citrate	NTD	SARS-CoV and SARS-CoV-2	>10	>10	>10	>10
61	DH1088	Ab026245_LS/293i/Citrate	no binding	SARS-CoV-2	>10	>10	>10	>10
62	DH1073	Ab026258_LS/293i/Citrate	RBD	SARS-CoV, SARS-CoV-2, and bat CoVs	0.8088	0.0161	0.267	>10
64	DH1235	Ab026319_LS/293i/Citrate	RBD	SARS-CoV, SARS-CoV-2, and bat CoVs	0.1226	0.0403	0.0602	>10
65	#N/A	Ab026336_LS/293i/Citrate	RBD	SARS-CoV and SARS-CoV-2	>10	>10	>10	>10
66	DH1193	Ab712053_LS/293i/Citrate	RBD	SARS-CoV and SARS-CoV-2	4.345	>10	>10	>10
67	DH1152	Ab712109_LS/293i/Citrate	RBD	SARS-CoV and SARS-CoV-2	>10	>10	>10	>10
68	DH1171	Ab712113_LS/293i/Citrate	NTD	SARS-CoV and SARS-CoV-2	>10	>10	>10	>10
69	DH1109	Ab712156_LS/293i/Citrate	RBD	SARS-CoV and SARS-CoV-2	>10	>10	>10	>10
70	DH1208	Ab712166_LS/293i/Citrate	RBD	SARS-CoV and SARS-CoV-2	>10	>10	>10	>10
71	DH1166	Ab712215_LS/293i/Citrate	RBD	SARS-CoV and SARS-CoV-2	>10	>10	>10	>10
72	DH1191	Ab712224_LS/293i/Citrate	RBD	SARS-CoV and SARS-CoV-2	>10	>10	>10	>10
73	DH1120	Ab712294_LS/293i/Citrate	RBD	SARS-CoV and SARS-CoV-2	>10	>10	>10	>10
74	DH1110	Ab712312_LS/293i/Citrate	NTD	SARS-CoV and SARS-CoV-2	>10	>10	>10	>10
75	DH1106	Ab712366_LS/293i/Citrate	NTD	SARS-CoV and SARS-CoV-2	>10	>10	>10	>10
76	DH1112	Ab712370_LS/293i/Citrate	RBD	SARS-CoV and SARS-CoV-2	>10	0.0023	0.1617	>10
77	DH1117	Ab712376_LS/293i/Citrate	RBD	SARS-CoV and SARS-CoV-2	>10	>10	>10	>10
78	DH1115	Ab712378_LS/293i/Citrate	RBD	SARS-CoV and SARS-CoV-2	>10	0.0083	0.1614	>10
79	DH1093	Ab712381_LS/293i/Citrate	NTD	SARS-CoV and SARS-CoV-2	>10	>10	>10	>10
80	DH1095	Ab712402_LS/293i/Citrate	RBD	SARS-CoV	>10	>10	>10	>10
81	DH1113	Ab712404_LS/293i/Citrate	RBD	SARS-CoV and SARS-CoV-2	>10	>10	>10	>10
82	DH1114	Ab712407_LS/293i/Citrate	NTD	SARS-CoV and SARS-CoV-2	>10	>10	>10	>10
84	DH1098	Ab712416_LS/293i/Citrate	RBD	SARS-CoV and SARS-CoV-2	>10	0.0052	0.0318	>10
85	DH1101	Ab712423_LS/293i/Citrate	RBD	SARS-CoV and SARS-CoV-2	>10	0.0012	>10	>10
86	#N/A	Ab712561_LS/293i/Citrate	RBD	SARS-CoV and SARS-CoV-2	>10	0.0399	0.4312	>10
87	#N/A	Ab712572_LS/293i/Citrate	RBD	SARS-CoV and SARS-CoV-2	>10	>10	>10	>10
88	#N/A	Ab712584_LS/293i/Citrate	RBD	SARS-CoV and SARS-CoV-2	>10	>10	>10	>10
89	#N/A	Ab712585_LS/293i/Citrate	RBD	SARS-CoV and SARS-CoV-2	>10	>10	>10	>10
90	#N/A	Ab712588_LS/293i/Citrate	RBD	SARS-CoV and SARS-CoV-2	>10	>10	>10	>10
91	#N/A	Ab712614L_LS/293i/Citrate	RBD	SARS-CoV and SARS-CoV-2	>10	>10	>10	>10
92	#N/A	Ab712617_LS/293i/Citrate	RBD	SARS-CoV and SARS-CoV-2	>10	>10	>10	>10
93	#N/A	Ab712618_LS/293i/Citrate	RBD	SARS-CoV and SARS-CoV-2	9.877	>10	>10	>10

Supplemental Table 2: Immunogenetic characteristics of broadly cross-reactive mAbs

DH#	Antibody ID	Binding Specificity	Cross Reactivity	Antibody Gene Analysis									
				Donor ID	Time Point	HCDR3 Length	Heavy chain mutation	VH_Gene	JH_Gene	LCDR3 Length	Light chain mutation	VL_Gene	JL_Gene
DH1235	Ab026319_LS	RBD	SARS-CoV-1	SARS-CoV-2 convalescent	Day 36	21	1.68	IGHV3-48	IGHJ4	9	1.75	IGLV4-60	IGLJ2
DH1073	Ab026258_LS	RBD	SARS-CoV-1	SARS-CoV convalescent	Year 17	15	9.06	IGHV1-46	IGHJ6	11	2.92	IGKV3-11	IGKJ1
DH1046	Ab026204_LS	RBD	SARS-CoV, PCoV GXP4L, Bat CoV RsSHC014, Bat CoV RaTG13	SARS-CoV convalescent	Year 17	24	4.70	IGHV3-23	IGHJ6	9	3.65	IGKV1-5	IGKJ2
DH1047	Ab712384_LS	RBD	SARS-CoV, PCoV GXP4L, Bat CoV RsSHC014, Bat CoV RaTG13	SARS-CoV convalescent	Year 17	24	8.05	IGHV1-46	IGHJ4	9	2.05	IGKV4-1	IGKJ1